Spring 1-1-2015

Proximal Blade Twist Feedback Control for Heliogyro Solar Sails

Sarah Mitchell Smith
University of Colorado at Boulder, sarah.m.smith5@gmail.com

Proximal Blade Twist Feedback Control for Heliogyro Solar Sails

by

Sarah Mitchell Smith

B.S., University of Colorado at Boulder, 2013

A thesis submitted to the

Faculty of the Graduate School of the

University of Colorado in partial fulfillment

of the requirements for the degree of

Master of Science

Department of Aerospace Engineering Sciences

2015

This thesis entitled:
Proximal Blade Twist Feedback Control for Heliogyro Solar Sails
written by Sarah Mitchell Smith
has been approved for the Department of Aerospace Engineering Sciences

_____

Dr. Dale Lawrence

_____

Dr. Eric Frew

Date _____

The final copy of this thesis has been examined by the signatories, and we find that both the content and the form meet acceptable presentation standards of scholarly work in the above mentioned discipline.

Smith, Sarah Mitchell (M.S., Aerospace Engineering)

Proximal Blade Twist Feedback Control for Heliogyro Solar Sails

Thesis directed by Dr. Dale Lawrence

A heliogyro spacecraft is a specific type of solar sail that generates thrust from the reflection of solar photons. It consists of multiple long (200 to 600 meters), thin blades, similar to a helicopter. The heliogyro's blades remain in tension by spinning around the central hub of the spacecraft. The individual blades are pitched collectively or cyclically to produce the desired maneuver profile. The propellant-free heliogyro is a long-duration sustainable spacecraft whose maneuverability allows it to attain previously inaccessible orbits for traditional spacecraft. The blades are constructed from thin Mylar sheets, approximately 2.5 μm thick, which have very little inherent damping making it necessary to include some other way of attenuating blade vibration caused by maneuvering. The most common approach is to incorporate damping through the root pitch actuator. However, due to the small root pitch control torques required, on the order of 2 μNm, compared to the large friction torques associated with a root pitch actuator, it is challenging to design a root control system that takes friction into account and can still add damping to the blade.

The purpose of this research is to address the limitations of current control designs for a heliogyro spacecraft and to develop a physically realizable root pitch controller that effectively damps the torsional structural modes of a single heliogyro blade. Classical control theory in conjunction with impedance control techniques are used to design a position-source root pitch controller to dominate friction with high gains, wrapped with an outer loop that adds damping to the blade by sensing differential twist outboard of the blade root.

First, modal parameter characterization experiments were performed on a small-scale heliogyro blade in a high vacuum chamber to determine a how much inherent damping is present in the blade, which drove the selection of the damping constant used in the membrane ladder finite element model of the blade. The experimental damping ratio of the lowest frequency torsional

mode is on the order of 0.005%, meaning there is almost no inherent damping in the blade. Next, the proximal blade twist feedback control design was successful in overcoming friction in the root actuator and added damping to the blade. The damping ratio for the lowest frequency torsional mode was increased from 0.001% to 0.09%, which is a significant amount for a heliogyro spacecraft. Finally, the camera sensor used for the proximal differential twist measurement proved to be feasible and quantization from these measurements only decreased the damping ratio to 0.075%.

This research provides the first indication that a physically realizable blade root controller can deal with friction in an effective way, thus taking a step towards advancing the technology readiness level of the heliogyro spacecraft.

Acknowledgements

I would like to acknowledge Dale Lawrence, Daniel Guerrant, Keats Wilkie, and Jay Warren for their assistance and guidance with this research.

Contents

Tables

Table

Figures

Figure

Chapter 1

Introduction and Literature Review

The concept of solar sailing as a means to travel through space was first conceived by the astronomer Johannes Kepler some 400 years ago. His concept utilized a solar "breeze" to move the sail through space [1]. Since then it has been shown that solar photons, reflecting off the sail's large mirrored surface, can transfer their momentum to the sail, thus producing an acceleration on the spacecraft. When a photon impacts a perfectly specular reflective sail, it results in incident and reaction forces exerted on the sail, as shown in Figure 1.1. The sum of the forces yields a total force

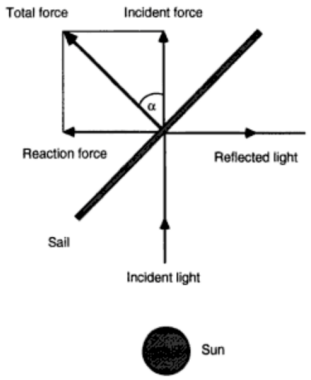

Figure 1.1: Transfer of momentum to a solar sail by photons [2]

acting normal to the sail. The sail pitch angle, α, defines the orientation of the sail and total force, or thrust, vector relative to the Sun-line. By adjusting the sail's orientation relative to the Sun-line, the direction and magnitude of the thrust changes, thus allowing the sail to change orientation and acceleration [2]. Solar sail technology is beneficial for missions that require a large change in velocity, such as longer interplanetary missions and space weather warning systems between the Earth and Sun. The large amounts of fuel together with mass restrictions have been limiting factors for using traditional chemical propulsion on these missions. In addition, the sail experiences constant thrust, that allows it to reach larger velocities over time, making solar sails ideal for longer duration missions.

The first solar sail to be flown in space was the Japanese Aerospace Exploration Agency's (JAXA) Interplanetary Kite-craft Accelerated by Radiation of the Sun (IKAROS), in 2010. The mission demonstrated that a solar sail is capable of producing a small, but extant, 0.007 mm/s^2 characteristic acceleration on a spacecraft [3]. The characteristic acceleration is a universal metric for solar sails "defined as the solar radiation pressure acceleration experienced by a solar sail facing the Sun at a distance of one astronomical unit (au), the mean distance of the Earth from the Sun" [2]. IKAROS is a spinning square sail, meaning it uses the centrifugal forces caused by spinning to flatten the sail [4]. This sail configuration is one of three main ideas for solar sail design. The spinning square or disc sail configuration does not require structural booms to tension the sail. The attitude of the spinning sail is controlled by changing the center of mass relative to the constant center of pressure, which produces a torque on the spacecraft that precesses the spin axis of the sail. The other traditional sail design is the non-spinning square sail that uses four structural booms to deploy and flatten four sail quadrants. Unlike the spinning sail, the booms add complexity to the deployment and storage of the sail. Again, the attitude can be controlled by moving the center of mass or by tilting reflective vanes located at each corner of the sail [2].

The third solar sail configuration, known as the heliogyro, was first introduced by Richard MacNeal in the 1960s as a proposed spacecraft to rendezvous with Halley's Comet. The heliogyro consists of multiple long and thin blades rotating about the central hub of the spacecraft as seen in

Figure 1.2. The blade material is made from aluminized Mylar sheets that can be as small as 2.5

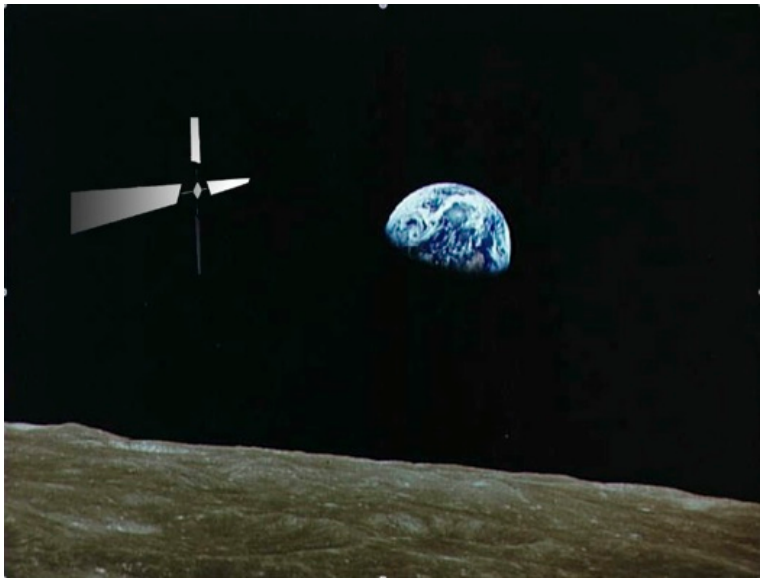

Figure 1.2: Artist's depiction of a heliogyro in orbit [5]

μm thick. The heliogyro concept requires less support structure than a traditional solar sail since the centrifugal forces help to deploy and maintain a rigid blade shape [6]. The individual blades are pitched collectively or cyclically to produce forces and moments on the sailcraft to achieve a desired maneuver profile [7]. The three basic pitch profiles consist of collective, cyclic and half-p maneuvers. A collective maneuver holds all the blades at the same pitch angle, allowing the sailcraft to produce spin up or down moments and a spin-averaged thrust normal to the sail plane, again assuming perfectly specular reflection. A cyclic maneuver commands each blade to follow a sine curve with a period equal to one revolution of the spinning sailcraft, which produces a significant amount of in-plane thrust, something a flat solar sail cannot do. The half-p maneuver is a cyclic maneuver over the period of two revolutions. The half-p produces an in-plane moment used to precess the spin axis of the heliogyro thus controlling the orientation. In addition, it generates thrust normal to the sail plane [3]. Due to the large scale of the heliogyro concept—some have blades designed to be 600 meters long—together with the difficulty of working with the thin blade material, much of the heliogyro research has focussed on understanding blade structural dynamics,

along with methods for packaging and deployment of the blades.

Relatively little work has been done to address the problem of heliogyro blade control. When the heliogyro was first considered for the mission to Halley's Comet, MacNeal studied the blade's structural dynamics and intrinsic damping. Using previous knowledge from helicopter dynamics, he derived uncoupled, one-dimensional equations of motion for the blade's twist (pitch), θ, vertical (out-plane or flap) deflection, ω, and in-plane (lead-lag) deflection, u. The boundary conditions used for the partial differential equations assume no concentrated forces or moments are applied at the outboard end of the blade. The boundary condition at the root of the blade assumes the pitch angle, θ, follows the motion designated by the root control actuator [8].

From these uncoupled equations of motion, MacNeal determined the blade's natural modes and response to vibrational excitation. It was shown that the dimensionless homogenous equations of motion have solutions in the form of Legendre polynomials, and the vibrational mode frequencies for twist, vertical displacement and in-plane displacement were found. Table 1.1 shows the modal frequencies for the first four modes of each type of motion for a zero displacement boundary condition at the root, meaning that the parameter n in the Legendre polynomial is an odd integer [8].

Table 1.1: Uncoupled blade frequencies [8]

n	Twist	Vertical	Inplane
1	$\sqrt{2} = 1.414$	1.0	0
3	$\sqrt{7} = 2.646$	$\sqrt{6} = 2.449$	$\sqrt{5} = 2.236$
5	$\sqrt{16} = 4.000$	$\sqrt{15} = 3.873$	$\sqrt{14} = 3.742$
7	$\sqrt{29} = 5.385$	$\sqrt{28} = 5.291$	$\sqrt{26} = 5.099$

It is important to note that the values in the table are the scaled vibration frequencies in cycles per revolution, given by $\bar{\omega} = \frac{\omega}{\Omega}$.

A key characteristic of the heliogyro is that the modal frequencies have a fixed relationship to the rotor speed even if the blade's size or material properties change. The modal frequencies will shift slightly if tip weights or tapering of the blade is added. Due to the relationship between

frequency and rotor speed, MacNeal noted that the twist mode at $\sqrt{2}$/rev could cause issues with resonant excitation: root motions could deposit energy into this mode, and if no damping were present, blade deflections could grow to unacceptable amplitudes. MacNeal recognized that there is likely not enough inherent damping in the blade, and he suggested that the pitch (twist), in-plane (lead-lag) and vertical (out-plane or flap) modes should be damped passively with mechanical damping devices [8]. His design used a spring and dashpot in parallel, situated in series between the root control actuator and the blade, as shown in Figure 1.3.

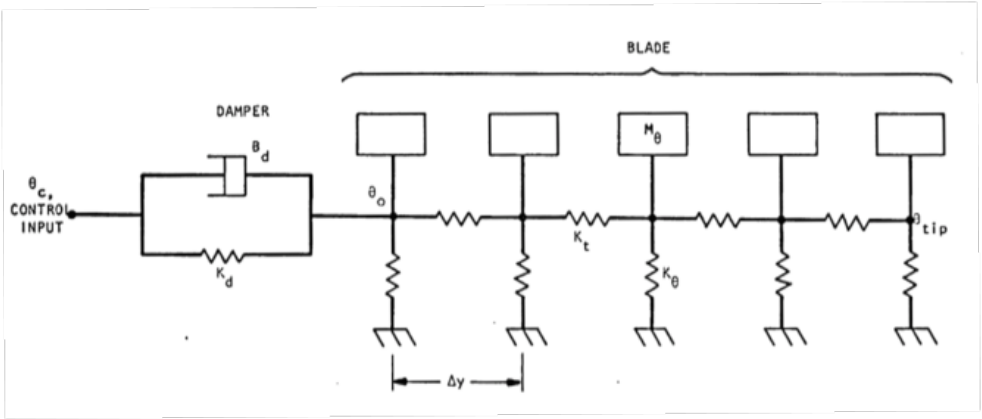

Figure 1.3: MacNeal's idealized model blade pitch control and damping [8]

To address the structural dynamics concern of unbounded blade vibration due to root motion excitation (away from the structural resonance frequency), a parametric study was performed to determine the optimum physical magnitude of the spring and damper, denoted as the control stiffness, K_d, and control damping, B_d, respectively. In order to determine the effect of the passive control system on the torsional damping, MacNeal analyzed the blade's response to a collective pitch input denoted θ_{co}, which is formulated as a ramp input that reaches its final pitch amplitude at half a revolution [8]. The blade's response at the root and tip, both normalized by θ_{co}, are shown in Figure 1.4 and Figure 1.5.

As expected, the blade's root is more responsive than the tip to the control input. The pitch oscillations at the root settle faster than the oscillations at the tip but both locations still show the lowest frequency mode at $\sqrt{2}$ cycles per revolution in the response. The effects of the damper

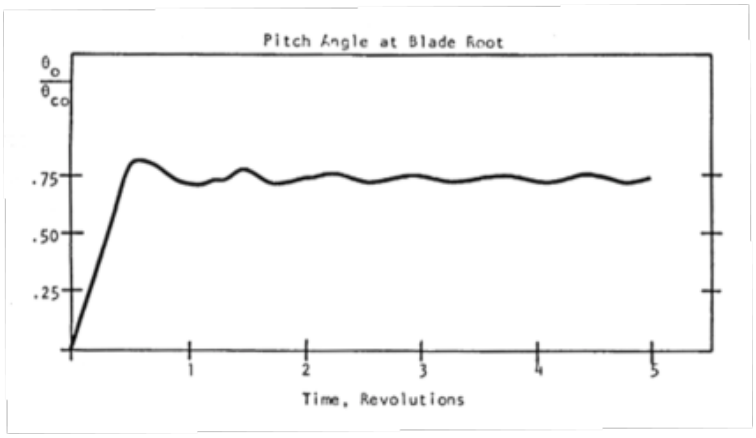

Figure 1.4: Blade's torsional root response to collective input [8]

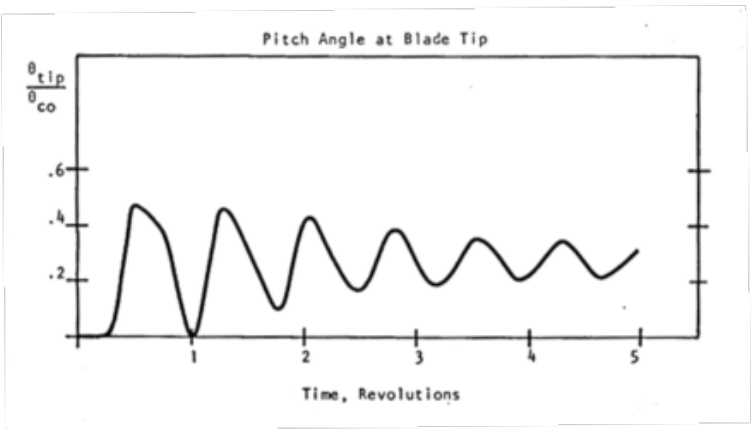

Figure 1.5: Blade's torsional tip response to collective input [8]

on the torsional vibration modal frequencies are depicted in Table 1.2. The frequency of the two

Table 1.2: Frequencies for blade twist modes with and without a control damper [8]

n	Twist Frequency without Control Damper (cycles/rev.)	Twist Frequency with Control Damper (cycles/rev.)
1	$\sqrt{2} = 1.414$	$\sqrt{2} = 1.368$
3	$\sqrt{7} = 2.646$	$\sqrt{7} = 2.618$
5	$\sqrt{16} = 4.000$	$\sqrt{16} = 4.022$
7	$\sqrt{29} = 5.385$	$\sqrt{29} = 5.455$

lowest torsional modes are reduced with the addition of the control damper. MacNeal attributes the increase in frequency of the two higher modes to the finite element approximation [8].

Through the design of the pitch damping mechanism, MacNeal concluded that the control moment is extremely small due to the low frequency of blade pitch actuation [8]. He recognized that the root pitch actuator will be extremely sensitive to friction in this mechanism, but did not suggest any mitigating strategies. Together with the difficulty of implementing passive mechanical damping on a spacecraft in general, but even more so at the very low damping constants required here, the practicality of this passive damping approach is dubious.

An alternative would be to provide active damping at the root, where sensed motions are applied in a feedback control system to the root actuator to produce a damping effect. Daniel Guerrant performed a preliminary study on an idealized feedback control system based on MacNeal's spring-damper design at the root. He derived uncoupled, one-dimensional equations of motion for the blade twist using a membrane ladder finite element model. Guerrant's idealized controller uses proportional/derivative/feed-forward compensation with a torque-source motor at the root. The goal of the controller is for the root to track the reference blade pitch maneuver and to add damping to the blade [3].

A baseline control law was used for easy comparison to MacNeal's passive damping mechanism and for establishing the maximum performance levels of the controller. The baseline design assumes a simplified plant with no material damping and an ideal controller, meaning it has infi-

nite bandwidth, introduces no additional dynamics into the system and uses an exactly accurate differentiator. The control law is given by the following equation,

$$M_{root} = K_p(\theta_{ref_1} - \theta_1) + K_d(\dot{\theta}_{ref_1} - \dot{\theta}_1) + K_{ff}\theta_{ref_1} \tag{1.1}$$

where K_p, K_d, K_{ff} are the controller's proportional, derivative and feed-forward gains, respectively. The reference pitch input at the root (rad) and it's angular velocity (rad/s) are given by θ_{ref_1} and $\dot{\theta}_{ref_1}$. The actual pitch angle at the root (rad) and the root's angular velocity (rad/s) are denoted as θ_1 and $\dot{\theta}_1$. The proportional gain is set to the root impedance at the reference input frequency. By setting K_p to this value, the root actuator stiffness (or real part of the controller impedance) is matched to the steady-state blade impedance at the root. This impedance matching will allow the root to extract the maximum energy from waves traveling along the blade caused by maneuver changes. MacNeal's passive damper cannot implement a feed forward term, therefore, K_{ff} is an immediate improvement on the previous design. By matching K_{ff} to the root impedance the steady-state root tracking error is eliminated for reference pitch frequencies below the frequency of the blade's first mode. Finally, the derivative gain is determined empirically by simulating a cyclic maneuver and observing which K_d value results in the fastest settling time [3]. The following table shows the optimized controller parameters used by Guerrant for each maneuver type.

Table 1.3: Summary of Guerrant's optimized controller parameters [3]

$Maneuver$	$K_p, K_{ff}(Nm/rad)$	$K_d(Nm/rad)$
Collective	2.62e-5	9e-4
Half-p	2.12e-5	9e-4
Cyclic	0	9e-4

Figure 1.6 depicts the the pitch profile of the entire blade (left sub-figures) and the reference, root and tip pitch (right sub-figure). Guerrant also indicates the settling time on all figures. With Guerrant's idealized controller the blade settles within one revolution of the heliogyro's spinning hub for all three maneuvers, which is five times faster than MacNeal's design. This improvement in settling time shows that damping is actively added to the blade with a feedback control system

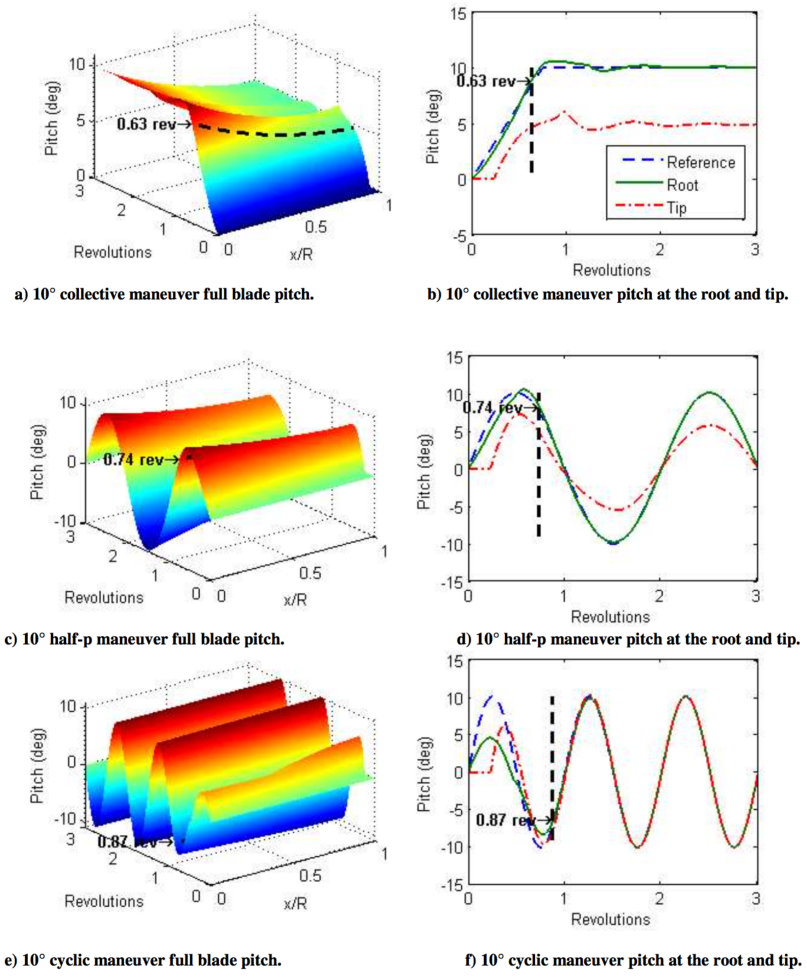

a) 10° collective maneuver full blade pitch.

b) 10° collective maneuver pitch at the root and tip.

c) 10° half-p maneuver full blade pitch.

d) 10° half-p maneuver pitch at the root and tip.

e) 10° cyclic maneuver full blade pitch.

f) 10° cyclic maneuver pitch at the root and tip.

Figure 1.6: Guerrant's baseline root controller performance for collective, half-p and cyclic maneuvers [3]

and torque-source actuator at the root. In addition, the feed-forward term eliminates the steady-state error in contrast to MacNeal's design that experienced a 25% steady-state error for collective maneuvers. However, this performance is achieved with an idealized controller. Guerrant went on to simulate the phase loss experienced by a realistic controller by adding a lag block to his simulation. He found that an actuator bandwidth of 3 cycles/rev (0.017 Hz) is required to achieve a settling time under four revolutions. Guerrant's initial study into active root control improved upon MacNeal's passive damping mechanism but did not focus on the concern to overcome friction in the root actuator [3].

Richard Blomquist also explored the idea of root pitch control for a heliogyro. Blomquist's goal for his blade pitch control design was to minimize the differential twist between the blade root and tip while ensuring the root tracks the reference input. Despite his acknowledgment that the force required to pitch the blade is far below the friction forces in a root actuator, he neglects to solve the problem directly. Blomquist advocates for a collocated sensor at the root to detect blade pitch since any sensors placed along the thin blade material would be complicated to integrate. His proposed controller design, shown in Figure 1.7, uses dual root actuators in series [9].

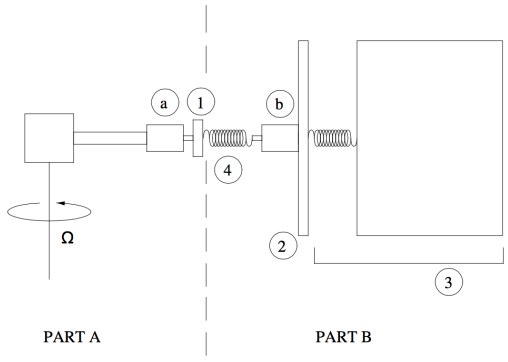

1. Coupler.
2. Blade Root Holder.
3. Blade
4. Spiral Spring.
a. Main Actuator (gear motor).
b. Secondary Actuator.

Figure 1.7: Blomquist's dual actuator root pitch controller [9]

The main actuator consists of a 10:1 geared motor connected in series to a coupler, spiral spring, secondary actuator, and blade root holder followed by the blade. The gear ratio used with the first motor is to prevent any backdriving but still allow the motor to respond quickly to changing input commands. The main actuator should follow the reference input closely, while the spiral spring and secondary actuator are used to extract energy from the blade and damp unwanted modes. When steady state is reached, the secondary actuator should follow the main actuator [9]. Results from Blomquist's control design are shown in Figure 1.8.

Blomquist designed his controller to have zero steady-state error, which is achieved by both the main and secondary actuators [9]. The main actuator settles within one-third a revolution of the central hub for all three maneuvers with the secondary actuator taking only slightly longer to settle. The blade lags behind the motion of the actuators but all higher frequency modes are damped. Blomquist's dual actuator root pitch controller successfully adds damping to the blade and provides redundancy with two actuators, in case one should fail. However, the control design is not physically realizable because it lacks the means to overcome friction in both actuators.

The ways to add blade damping do not have to be confined to the root. In fact, JAXA's IKAROS mission used a spinning square sail with reflectivity control devices (RCDs) on the sail. Guerrant explored a similar concept for heliogyros by using a RCD damping control system. Specifically, he looked at using liquid crystals RCDs, similar to ones used on IKAROS. These flexible substrates are mounted to the blade tip, covering 10% of the blade's reflective surface. When applied with a voltage, their reflectivity state switches from primarily diffuse to specular reflection and vice versa [4]. A diagram of the blade and RCD configuration is shown in Figure 1.9.

Each RCD segment shown in the diagram is controlled independently. There is an RCD on the leading and trailing edge, separated by a thin film solar cell, which is used to power the control system. By switching on and off the specular and diffuse reflectivity states of the RCDs, a difference in solar radiation pressure is generated, thus producing a torsional moment on the blade. The blade pitch control is still implemented with a root controller but the RCDs allow damping of unwanted torsional motions at the tip. However, the use of RCDs double the spacecraft's mass,

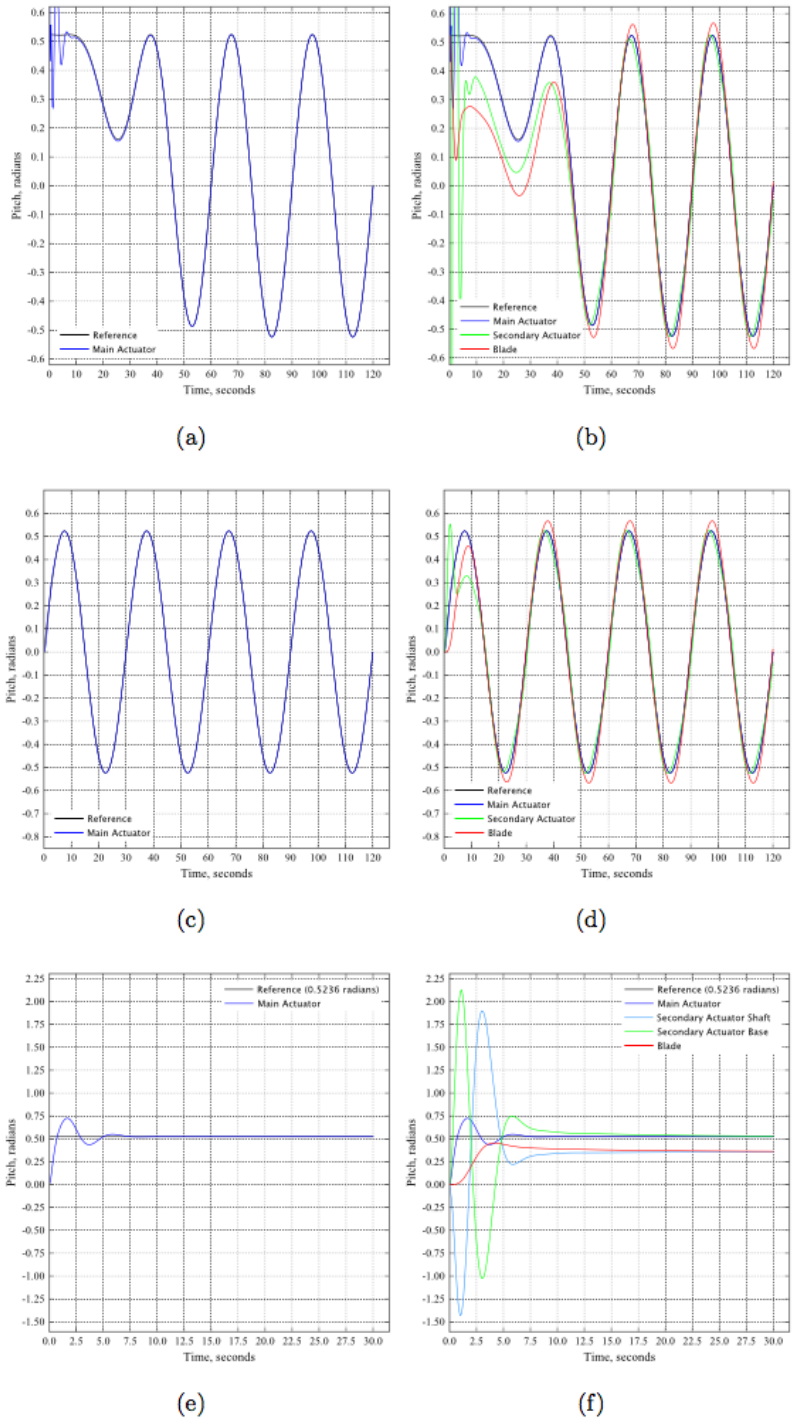

Figure 1.8: Blomquist's dual actuator root pitch controller tracking reference input. (a) and (b) are collective to cyclic transition, (c) and (d) are cyclic maneuvers and (e) and (f) are step inputs [9].

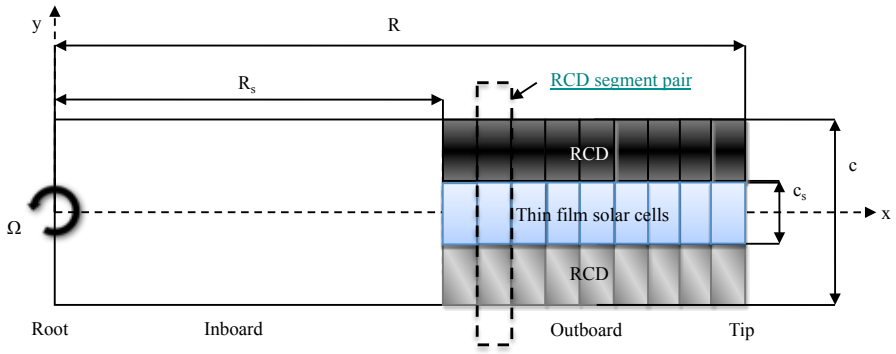

Figure 1.9: Configuration of a heliogyro blade with reflectivity control devices [4]

thus reducing the characteristic acceleration. By decreasing the RCD's thickness and increasing the difference between the diffuse and specular reflectivity states, the overall control performance could be improved by 200%. The difference in reflectivity states have a large affect on maneuver settling times. For instance, settling times decrease by 50% by doubling the difference in on/off reflectivity states and the characteristic acceleration increases by 63%. On the other hand, halving the RCD thickness reduces maneuver settling time by 35% percent but increases the characteristic acceleration by 127%. If advancements in technology improve upon current RCDs' thickness and on/off reflectivity differences, using RCDs simultaneously with a root feedback control system could be beneficial. However, at the current stage, the benefits from using RCDs do not outweigh their negative aspects, such as added mass and power requirements and the complexity of integration [4].

1.1 Research Questions

Although the groundwork for heliogyro control theory has been laid by MacNeal, Blomquist and Guerrant, the critical practical problems of friction are overlooked. This master's thesis uses Guerrant's linear rope ladder model for twist motion to design and simulate a physically realizable root pitch controller that damps twist structural modes of a single blade heliogyro. The approach taken to accomplish this begins with the linearized damping constant in the blade dynamics model.

In order to have a realistic and representative model for the blade's behavior in space, the damping constant was selected based on the modal parameter characterization experiments for a small scale heliogyro blade. Then, the control system is designed using classical control theory and impedance control techniques. A position-source root controller is developed that shows friction associated with a typical root pitch actuator can be ameliorated through high gain feedback control. Damping must still be added to the blade, which is implemented with the root actuator and a camera sensor in order to avoid added integration complexities with outboard damping mechanisms. An outer control loop is implemented around the high gain inner loop to add damping by sensing and feeding back the differential twist at a proximal point on the blade. A camera mounted to the root senses the differential twist and a photogrammetry model ensures the camera sensor has enough resolution to measure substantial differential twist.

The specific research questions addressed by this master's thesis include:

- What type of root control is needed to effectively damp the torsional structural modes of a single heliogyro blade and how can it be made physically realizable?
    - Is it possible to use a position-source root pitch controller to dominate friction with high gains, wrapped with an outer loop that adds damping to the blade by sensing differential twist outboard of the blade root and reinstating a "soft" mechanical impedance?
        - What are the limits of performance of this technique?

First, the analytical model used for the blade dynamics will be discussed along with a description of the blade's modal parameter characterization, which focused on experimentally determining the intrinsic damping in a heliogyro blade. Next, the controller design and simulation results will be analyzed followed by the implementation of outboard sensing with the photogrammetry model.

Chapter 2

Analytical Model

2.1 Membrane Ladder Finite Element Model

Guerrant derived the analytical model for blade dynamics used in this research. He developed a membrane-ladder finite element model that represents the blade as a series of connected segments or elements. Each element is composed of mass-less membranes connect by rigid rungs. The rungs contain the mass and moment of inertia for the blade element. The membrane-ladder has zero torsional stiffness, meaning it will not flatten once twisted, unless placed under tension. Guerrant's model differs from MacNeal's equations in that it includes the material damping term. The assumptions used for this model are:

- twist motions are uncoupled from flap and in-plane motions,
- cross-sections are uniform throughout the blade, meaning there is no camber in the blade,
- due to the magnitude of centrifugal stiffening effects, elastic stiffness is negligible,
- and the model is linearized using small angle approximations [3].

In order to develop the equations of motion for the blade, Guerrant began with a free-body diagram for a single element, or rung, n, of the blade, as shown in Figure 2.1. Applying Newton's law in rotation form, $M{=}J\alpha$, yields three different moments acting on the blade: gyroscopic, centrifugal and the moment due to material damping. The differential blade twist between elements, $\delta\theta_n$,

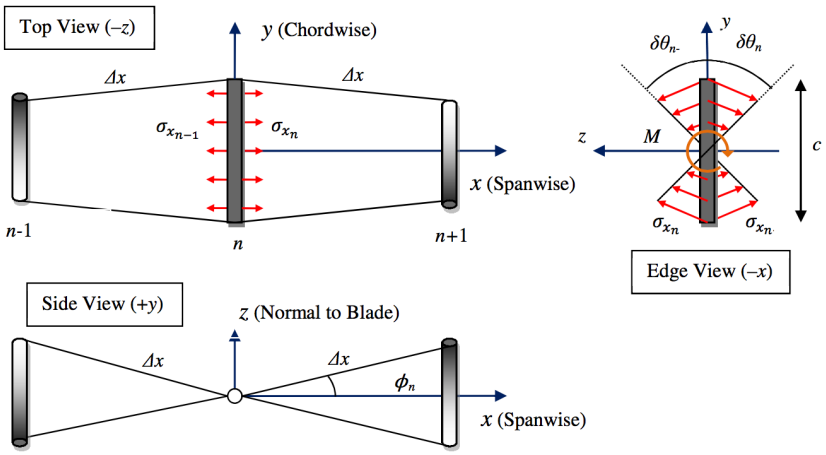

Figure 2.1: Free-body diagram of a single rung, n [3]

shown in Figure 2.1, is relatively small, therefore small-angle linearization is used in the equations of motion [3].

First, the gyroscopic moment, M_{gyro} is due to the centrifugal force that flattens the blade into the rotation plane to keep it from twisting, as shown in Equation 2.1,

$$M_{gyro_n} = -J_n \Omega^2 \sin\theta_n \cos\theta_n \cong -J_n \Omega^2 \theta_n = -K_{gyro_n} \theta_n. \tag{2.1}$$

In helicopter dynamics this is sometimes referred to as the tennis-racquet effect. The variable Ω (rad/s) signifies the heliogyro spin rate and θ_n (rad) is the twist or pitch of the element. Once small-angle linearization occurs, the equation consists of K_{gyro_n} (Nm/rad), which is the gyroscopic stiffness linearized about zero twist. The term J_n (kgm^2) is the mass moment of inertia for a single element, and is given by,

$$J_n = \frac{\Delta x}{12} \rho_{sail} h_{sail} c^3. \tag{2.2}$$

Δx (m) is the element's span. The blade's density (kg/m^3) and thickness (m) are given by ρ_{sail} and h_{sail}, respectively. The total blade chord (m) is represented by c [3].

Next, the centrifugal moment, M_{cent}, is found by integrating the centrifugal tension force,

$$F_{x_n} = \Omega^2 [\frac{1}{2} \rho_{sail} A_n (R^2 - x_n^2) + m_{tip} R] \tag{2.3}$$

$$\sigma_{x_n} = \frac{F_{x_n}}{A_n} \tag{2.4}$$

The force, F_{x_n}, is due to the blade stress, σ_{x_n}, acting primarily along the x-direction (spanwise) but when the blade is twisted, there is a component in the z-direction (out-of-plane) as well, which acts to flatten the membrane. The spanwise position is defined by x_n (m) and the tip mass is defined by m_{tip} (kg). A_n (m^2) is the elemental cross-sectional area and R (m) is the total blade span. The integral over the blade chord is shown in the following equation,

$$M_{cent_n} = \int_{-c/2}^{c/2} \sigma_{x_n} h y \sin\phi_n \, dy \tag{2.5}$$

and with the following small-angle linearization,

$$z = y \tan\delta\theta_n = \Delta x \sin\phi_n \tag{2.6}$$

$$\sin\phi_n \cong \frac{y \cdot \delta\theta_n}{\Delta x} \tag{2.7}$$

the integral is evaluated as,

$$M_{cent_n} = \frac{\sigma_{x_n} h c^3}{12\Delta x}(\theta_{n+1} - \theta_n) = \frac{\sigma_{x_n} I_n}{\Delta x}(\theta_{n+1} - \theta_n) = K_{cent_n}((\theta_{n+1} - \theta_n). \tag{2.8}$$

These equations include the in-plane chordwise position from the centerline, y (m), and the vertical membrane element deflection, ϕ_n (rad). The linearized centrifugal stiffness, K_{cent} (Nm/rad) is a product of the small-angle linearization. The area moment of inertia for an element about x is I_n (m^4),

$$I_n = \frac{h_{sail} c^3}{12}. \tag{2.9}$$

Since each element is attached at either end to another element (except for the first and last elements), the total centrifugal moment consists of the components at $n-1$, n, and $n+1$:

$$M_{cent_n} = K_{cent_n}(\theta_{n+1} - \theta_n) - K_{cent_{n-1}}(\theta_n - \theta_{n-1}) \tag{2.10}$$

When compared to the gyroscopic moment, Guerrant found that the centrifugal moment is two to three orders of magnitude greater, meaning it dominates the blade dynamics. Since Equation 2.10 is in terms of the differential twist between elements, which, as stated earlier, is small, the linearization is justified again [3].

Lastly, the material damping moment is defined in the following equation,

$$M_{damp} = d\frac{1}{\Delta x}[(\dot\theta_{n+1} - \dot\theta_n) - (\dot\theta_n - \dot\theta_{n-1})] = d\frac{1}{\Delta x}(\dot\theta_{n+1} - 2\dot\theta_n + \dot\theta_{n-1}) \tag{2.11}$$

which is caused by the stretching of the membrane elements. The linearized damping constant, d (Nm^2/rad), is determined experimentally and will be discussed in the next section. Similar to the centrifugal moment, M_{damp} has two components except for the root and tip elements [3].

By combining the moment equations, the final twist equation is obtained,

$$\sum M_x = J_n\ddot\theta_n = -K_{gyro_n}\theta_n + K_{cent_n}(\theta_{n+1} - \theta_n) - K_{cent_{n-1}}(\theta_n - \theta_{n-1}) + d\frac{1}{\Delta x}(\dot\theta_{n+1} - 2\dot\theta_n + \dot\theta_{n-1}) + M_{ext_n} \tag{2.12}$$

The only external torque in the equation is M_{ext}, which can be considered a control torque. The moment due to solar radiation pressure is zero since the forces act about the centerline, causing the moment to sum to zero for a twist only blade. This linear, time invariant equation can be converted to the following state-space model,

$$\dot{\mathbf{X}} = A\mathbf{X} + Bu$$
$$\mathbf{Y} = C\mathbf{X} + Du \tag{2.13}$$

$$\mathbf{X} = \begin{bmatrix} \boldsymbol{\theta} \\ \dot{\boldsymbol{\theta}} \end{bmatrix} \quad \mathbf{Y} = \begin{bmatrix} \theta_1 \\ \theta_6 \\ \dot{\theta}_1 \\ \theta_{tip} \end{bmatrix} \tag{2.14}$$

$$A = \begin{bmatrix} [0]_{N+1\times N+1} & [I]_{N+1\times N+1} \\ A^* & D^* \end{bmatrix}$$

$$A^* = \begin{bmatrix} -\frac{(K_{gyro_1}+K_{cent_1})}{J_1} & \frac{K_{cent_1}}{J_1} & & & \\ \ddots & \ddots & & & \\ & \frac{K_{cent_{n-1}}}{J_n} & -\frac{(K_{gyro_n}+K_{cent_n}+K_{cent_{n-1}})}{J_n} & \frac{K_{cent_n}}{J_n} & \\ & & \ddots & \ddots & \ddots \\ & & & \frac{K_{cent_N}}{J_{N+1}} & -\frac{(K_{gyro_{N+1}}+K_{cent_N})}{J_{N+1}} \end{bmatrix}$$

$$D^* = d\frac{1}{\Delta x}\begin{bmatrix} -\frac{1}{J_1} & \frac{1}{J_1} & & & \\ \ddots & \ddots & \ddots & & \\ & \frac{1}{J_n} & -\frac{2}{J_n} & \frac{1}{J_n} & \\ & & \ddots & \ddots & \ddots \\ & & & \frac{1}{J_{N+1}} & -\frac{1}{J_{N+1}} \end{bmatrix}$$

$$B = \begin{bmatrix} [0]_{N+1\times 1} \\ B^* \end{bmatrix} \quad u = M_{root} \tag{2.15}$$

$$C = \begin{bmatrix} 1 & [0]_{1\times N-1} & 0 & 0 & [0]_{1\times N} \\ [0]_{1\times 5} & 1 & [0]_{1\times N-5} & 0 & [0]_{1\times N} \\ 0 & [0]_{1\times N-1} & 0 & 1 & [0]_{1\times N} \\ 0 & [0]_{1\times N-1} & 1 & 0 & [0]_{1\times N} \end{bmatrix} \quad D = [0] \tag{2.16}$$

The subscript n corresponds to the element index while N is the total number of segments in the model [3]. It is important to note that the output includes θ_6 because this is the proximal point on the blade where differential twist is sensed and used in the feedback control law. The state-space form allows for easy integration into Simulink where the controller can be designed and time histories can be produced. The parameters used in the simulations are provided in the following table.

Table 2.1: Heliogyro blade simulation parameters

Number of elements (N)	19
Spin rate (Ω)	1/3 RPM
Blade span (R)	200 m
Blade chord (c)	0.75 m
Blade tip mass (m_{tip})	100 g
Sail thickness (h_{sail})	2.5 μm
Sail density (ρ_{sail})	1.5 g/cm^3
Linearized damping constant (d)	2e-6 Nm^{2}s/rad

Guerrant validated his membrane-ladder finite element model by comparing the twist blade frequencies to those MacNeal found, previously shown in Table 1.1. The zeros of the linear time invariant system correspond to the frequencies where root torque, M_{root}, causes no motion at the root but twists the blade elsewhere. These zeros also correspond to the modes in MacNeal's model. The comparison of the twist mode frequencies is shown in Table 2.2 [3].

The mode frequencies match closely for a larger number of elements but the 200 element case still accurately depicts the lower frequency modes. Due to the added complexity and computation time to run a simulation with a large number of elements, this research used 19 elements to prove

Table 2.2: Comparison of twist mode frequencies for Guerrent's membrane-ladder FEM and MacNeal's differential equations [3]

Mode	MacNeal	N = 200	N = 1000
ω_1	$\sqrt{2} = 1.414$	1.416	1.414
ω_2	$\sqrt{7} = 2.646$	2.661	2.649
ω_3	$\sqrt{16} = 4.000$	4.039	4.009
ω_4	$\sqrt{29} = 5.385$	5.457	5.402

a valid control design for a simplified model.

2.2 Modal Parameter Characterization for a Small Scale Heliogyro Blade

It turns out that all practical control systems actually *reduce* damping at high frequencies, so that *some* natural blade damping is needed to overcome this deficiency in control to result in a stable system. A physically realizable controller is subject to finite bandwidth and quantization of sensor measurements, which will cause phase loss in the system. This phase loss will reduce the blade damping. In addition, the controller cannot have control authority over all frequencies and has to "give up" at some point, which is where the intrinsic damping in the blade is important. The lower frequency twist modes have the largest amplitudes and therefore, are the ones the controller will damp. At the higher frequencies, when the controller no longer has authority, inherent damping in the blade is needed to reduce the amplitude of the higher frequency modes. This is especially critical for the specific control system designed in this research. By sensing at an outboard point on the blade and actuating at the root of the blade, a non-collocated controls problem is developed. In a traditional collocated problem the actuator and sensor are at the same location and for a lightly damped flexible structure, the poles and zeros of the system alternate along the imaginary axis as shown in Figure 2.2(a). However, with the non-collocation, a pole and zero are flipped, producing two poles in a row. The back to back poles result in a 180 degree phase loss and cause the Nyquist plot to have circles in both the positive and negative parts of the imaginary axis. The pole-zero map and Nyquist plot for the non-collocated case is depicted in Figure 2.2(b) and 2.2(d). When

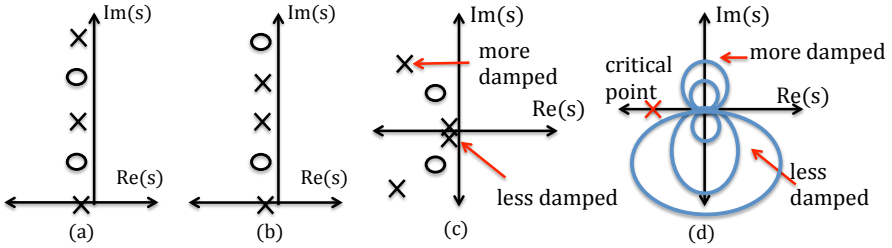

Figure 2.2: Pole-zero map for (a) collocated system (b) non-collocated system (c) plant with desired natural damping in the heliogyro blade and (d) non-collocated system Nyquist plot

designing the control system, a gain can be used to shrink the size of these circles but the amplitude of the low frequency modes will be quite large, making the circles along the negative imaginary axis close to the critical point. Therefore, some form of lead or lag compensation will be needed to rotate these circles away from the critical point, but this will also cause the top circles to rotate in the opposite direction, closer to the critical point. Some damping must already be present in the blade so the size of the top circles are smaller, meaning they will not encircle the critical point when rotated from some form of compensation. Figure 2.2(c) shows the specific pole zero map desired for the heliogyro blade dynamics plant. The poles at the higher frequencies are more damped than the lower frequency poles. This topic will be discussed more in Chapter 3.

The linearized damping constant is determined experimentally since it is effected by many variables, such as temperature [3]. Experiments performed at NASA Langley's Structural Dynamics Branch during an internship were used to characterize the modal parameters of a small-scale blade, specifically the natural frequencies of the mode shapes and their corresponding damping ratios.

Previous summer interns worked with a small-scale heliogyro blade to characterize its modal parameters in a vacuum chamber, which was used to simulate its behavior in a realistic space environment. Specifically, one prior student was investigating the relationship between the modal parameters and the pressure inside the vacuum chamber. In order to characterize this relationship, two test facilities were used to generate a wide range of pressures. The first was an eight-foot vacuum sphere shown in Figure 2.3 and the second was the high vacuum chamber in Figure 2.4 [10].

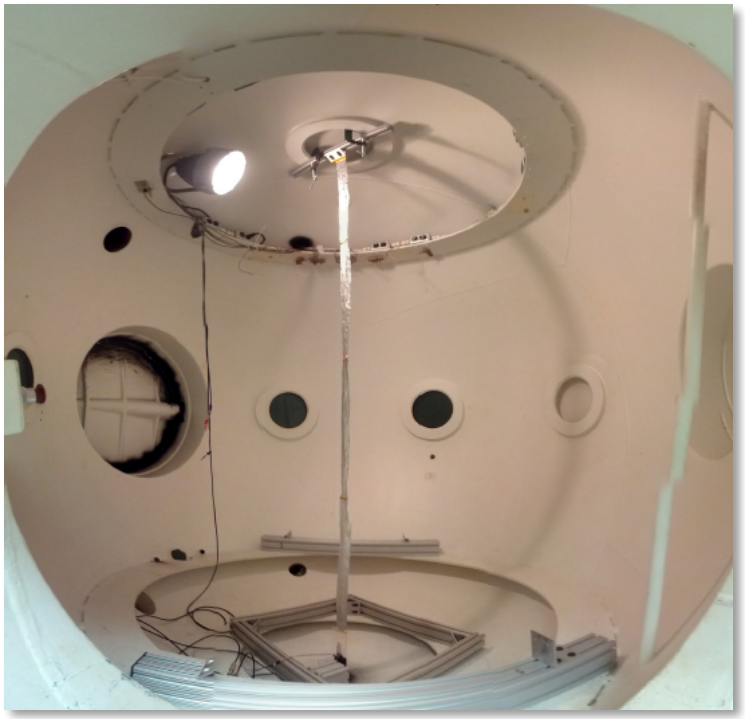

Figure 2.3: NASA Langley Structural Dynamics Branch's eight-foot vacuum sphere [10]

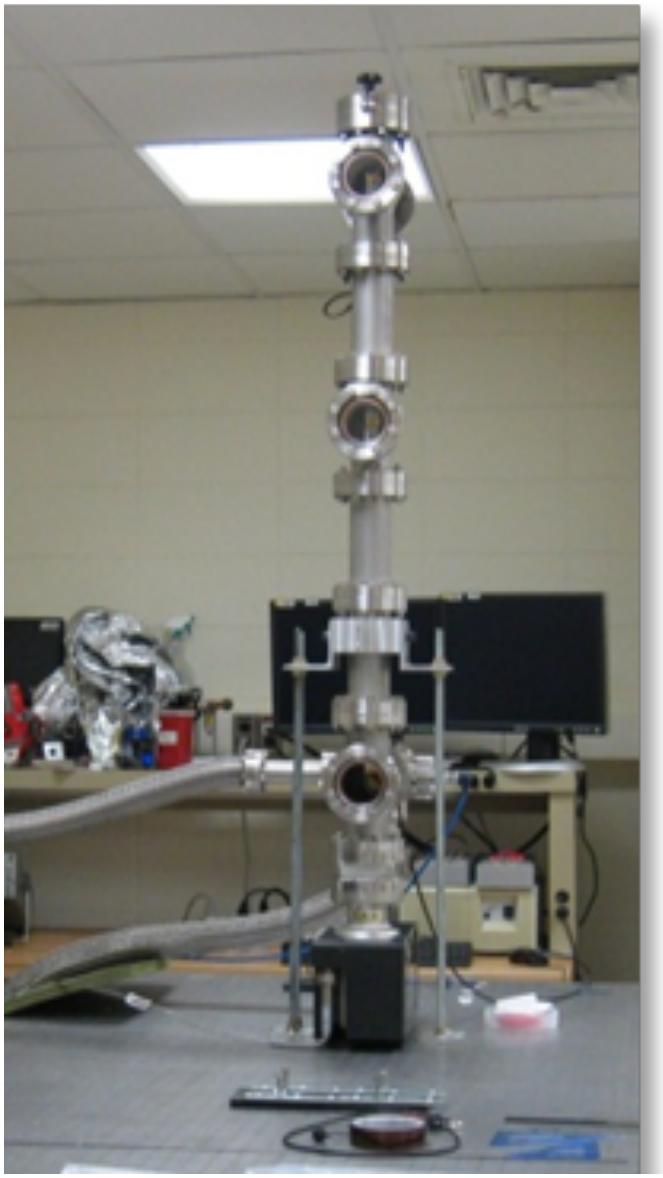

Figure 2.4: NASA Langley Structural Dynamics Branch's high vacuum chamber

The previous experiments showed there was a combined flap and twist mode at 0.57 Hz with a corresponding damping ratio of 0.024%. Tests performed at different pressures revealed that there was negligible change in the frequency of the combined mode for varying pressures, however, the percent damping ratio for the combined mode decreased as the pressure decreased, as seen in Figure 2.5. The experiments performed during my internship are the two data points from 2014.

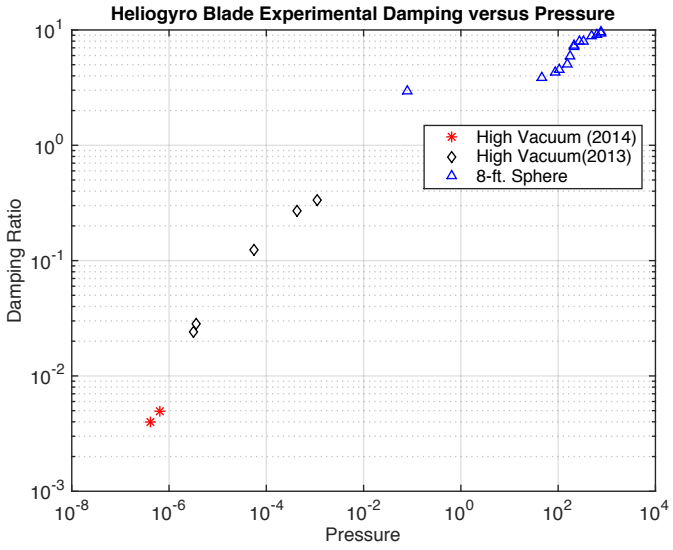

Figure 2.5: Pressure versus damping for small scale heliogyro blade

Due to time and facility limitations, only two experiments were performed in the high vacuum chamber at pressures around 10^{-7} torr. From the few experiments, it is uncertain whether the percent damping ratio is leveling off and no longer decreasing in value. More thorough experiments are needed to solidify confidence in the value of inherent damping in the blade.

The objectives for my research at NASA Langley included three main tasks. First, was to refine the testing procedure to collect the best possible data on the blade's free decay motion. This included understanding the signal generator, laser vibrometer, data acquisition parameters and system identification software. The second task was to characterize the new flap and twist actuator in the hopes to separate the combined flap and twist mode at 0.57 Hz into two distinct modes. Thirdly, experimental testing in the high vacuum chamber was to be performed on a rope ladder

and Mylar membrane blade to determine their modal parameters. Again, the most important question to answer was whether or not a more confident bound on the damping could be achieved through the blade characterization tests to be used in future analytical models.

2.2.1 Modal Parameter Characterization Experimental Procedure

There were two main experimental tests performed in order to complete the objectives, one being the actuator characterization and the other being the blade characterization test. The newest version of the flap and twist actuator is shown in Figure 2.6. The actuator was mounted on the test bench, outside of the high vacuum chamber. A Polytec Scanning Laser Vibrometer was used for this experiment along with a piezo amplifier. The concept of operations for this test is depicted in Figure 2.7. The Polytec software generated an excitation input signal, in this case a sine sweep from 0.1 Hz to 20 Hz at 3 volts amplitude. The signal then gets amplified by the piezo amplifier from 3 volts to around 300 volts, before being fed to the piezoelectric actuator. The input voltage transfers through the piezoelectric and causes the actuator to vibrate. The scanning laser vibrometer measures the velocity of two predefined scan points on the actuator, which is then recorded by the Polytec software and exported as a universal file. The time history of the actuator's velocity is loaded into MATLAB for post processing (i.e. filtering the data). In order to obtain the modal parameters from the experimental data, a system identification toolbox in MATLAB was used. Specifically, the System/Observer/Controller Identification Toolbox (SOCIT) created by Juang and Horta was used for system identification [11].

The blade characterization tests followed the same procedure as the actuator characterization except the velocity of the blades was measured and a different input signal was used. Two small-scale blades were tested, each 34.75 inches long and 1 inch wide. The first was the rope ladder blade. The edges of the rope ladder were fabricated from two pieces of sewing thread. There were four paper battens super glued to the sewing thread at the quarter points along the length of the blade. Two white dots were taped to the bottom batten of the blade at each corner to provide large scan points for the laser. The total weight of the rope ladder blade measured 0.164 grams.

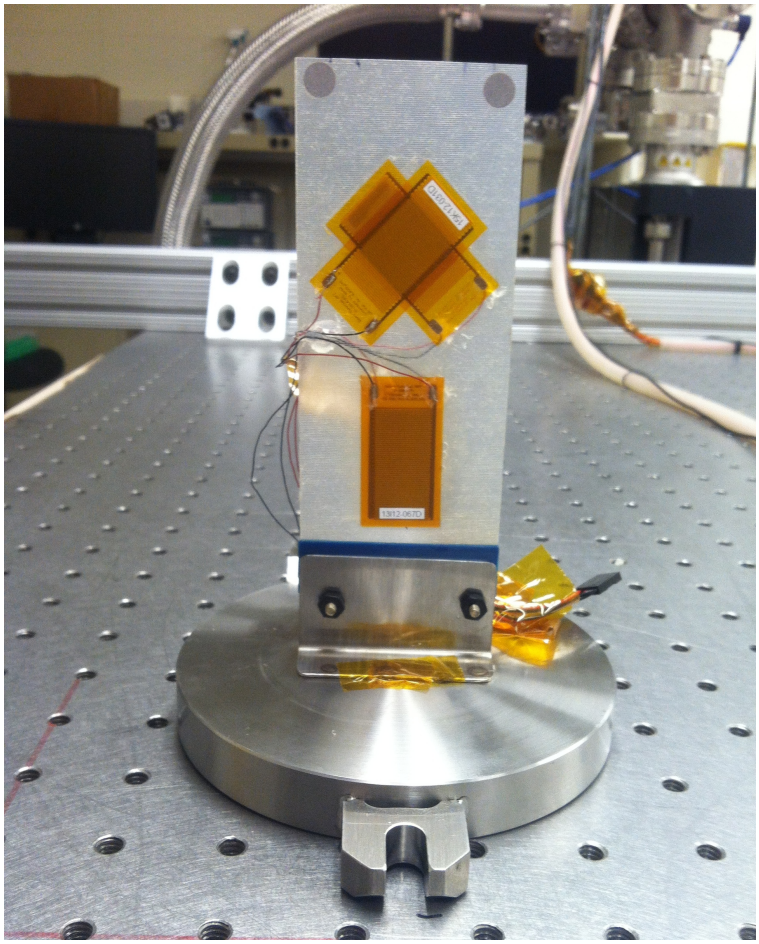

Figure 2.6: Flap and twist actuator

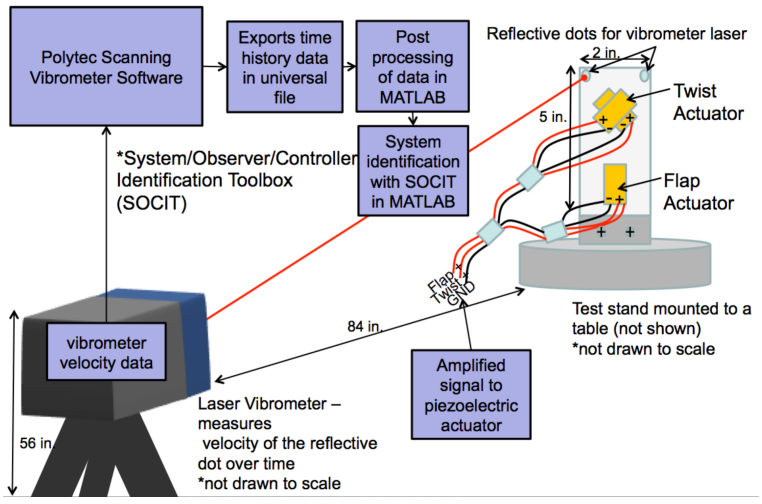

Figure 2.7: Actuator characterization procedure

A finite element model of the rope ladder blade was generated in Abaqus. The analytical model predicated the blade to have a flap and twist mode at 0.57 Hz. In addition, there were larger flap and twist modes at 1.73 Hz.

The second specimen was the Mylar membrane blade. The body of the blade was fabricated from aluminized Mylar. Four strips of paper were super glued to the blade to act as stiffening battens. Again, the battens were placed at the quarter points along the length of the blade. Two white dots, used as scanning targets were taped to the bottom batten. Just above the last batten, two lead split shot weights (used in fly fishing) were clasped to each edge of the blade. The extra weights were added to simulate a scaled down version of the force that a full-scale blade would experience during flight. The weight of the Mylar membrane blade was 5.45 grams. A finite element model was generated for the Mylar membrane blade as well. It predicated a flap and twist mode at 0.53 Hz.

Figure 2.8 depicts the MATLAB generated 0.57 Hz sine impulse signal at 3.5 volts used for the excitation input in the blade characterization tests. The input signal was amplified to around

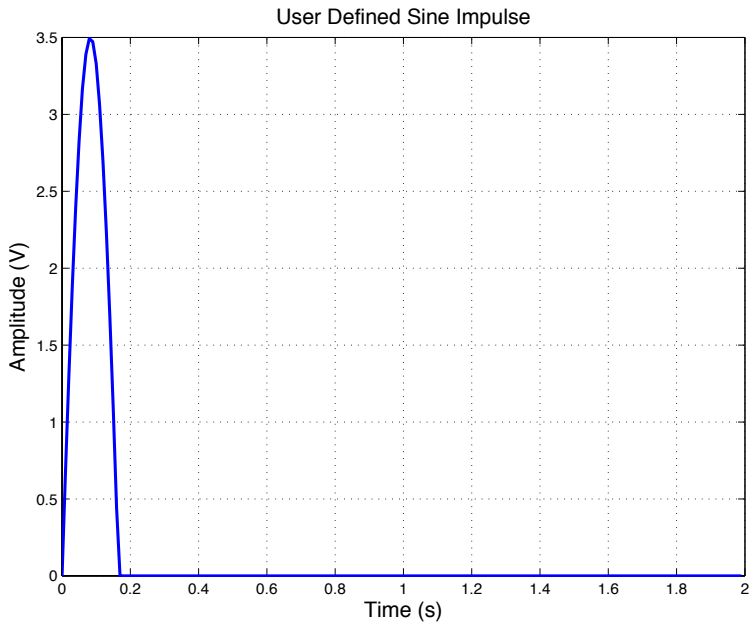

Figure 2.8: User defined sine impulse for blade characterization tests

350 volts before going into the actuator. The actuator was mounted to the lid of the high vacuum chamber, with the blade secured onto the end and left free to hang. The blade was installed so it did not touch the sides of the chamber. A viewing window on the high vacuum chamber allows the laser to scan the two points on the bottom batten of the blade. As stated previously, the velocity histories were exported as universal files and post processed in MATLAB using the SOCIT toolbox.

It should be noted that multiple tests were conducted in order to determine the best input signal to use as well as the best way to post process the experimental data. Initially, a sine sweep was used as the input signal for the blade characterization tests. However, it was found that not much was needed to excited the blade and that the free decay data produced the best results. Therefore, a user defined sine impulse was used for final testing where the blade was only excited for a short time period (0.167 seconds) but free decay data was recorded for longer periods of time (17 minutes). The amount of time free decay data could be logged was limited by the data acquisition hardware and software, making 17 minutes the maximum length of time for each test. Originally, the time history data was filtered through a bandpass filter to eliminate frequencies below 0.2 Hz and above 1 Hz. It was found that less filtering of the data yielded more reliable results from SOCIT.

2.2.2 Modal Parameter Characterization Experimental Results

The actuator characterization test gave insight into two different areas. First, it was found that the natural frequencies of the actuator itself were far above any frequencies expected from the blade. This was a good discovery because the input signal from the actuator would not be interfering with the blade's natural motion. Second, the actuator bench test showed the dual input piezoelectric would not be able to produce separate flap and twist motions. Due to the restricted time frame of the summer research, it was decided to continue the testing with the actuator but only supply power to the flap piezoelectric since the motions could not be separated.

The rope ladder blade was tested first. Again, the input signal in Figure 2.8 was used for the blade characterization tests. Figure 2.9 shows the raw velocity data and the decimated velocity

data for the first scan point on the rope ladder. The raw velocity data was decimated because the

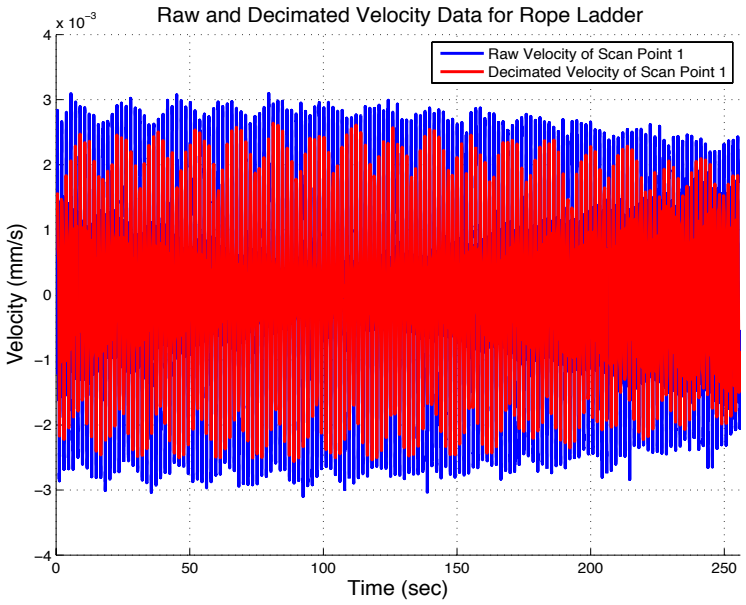

Figure 2.9: Rope ladder velocity data

original sampling frequency was 256 Hz. For optimum results, SOCIT requires that the input data be decimated such that the frequency range of interest is higher than 10% and lower than 75% of Nyquist frequency. For these tests the frequency range of interest was 0.1 to 2 Hz so the number of samples was reduced by a factor of 64 to get the decimated velocity data. Next the built-in MATLAB Fast Fourier transform function (fft.m) was used to take the FFT of the decimated velocity data, allowing the time domain data to be mapped into the frequency domain. The FFT of the rope ladder's decimated velocity data can be seen in Figure 2.10. By plotting the FFT, the dominant frequencies become visible making it easier for SOCIT to identify the 0.582 Hz and 1.742 Hz frequencies for the rope ladder.

It was found that SOCIT's modal parameter identification function in the frequency domain (modidfd.m) was better at identifying the real modes than the time domain function (modid.m). Tables 2.3 and 2.4 list the results from SOCIT and the finite element predictions previously mentioned.

SOCIT's frequencies match the analytical FEM frequencies with a 2% error for the lowest

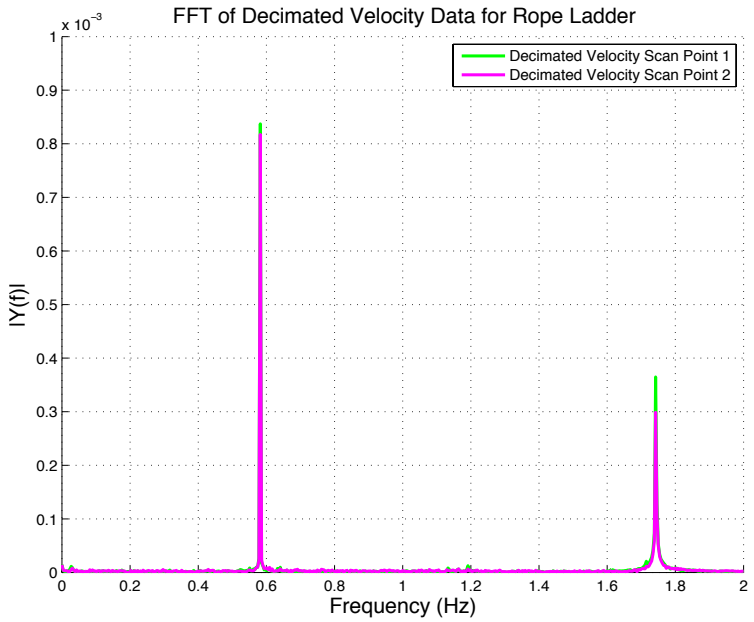

Figure 2.10: FFT of Decimated Velocity for Rope Ladder Blade

Table 2.3: Finite element predictions for rope ladder blade

Frequency (Hz)	**Mode Shape**
0.57	1st Flap Mode
0.57	1st Twist Mode
1.73	2nd Flap Mode
1.73	2nd Twist Mode

mode, which provides even more confidence that these are true natural frequencies for the rope ladder blade. The percent damping ratio was more variable, depending on the inputs into SOCIT but remained on the order of 0.01% to 0.001% damping. Therefore, the experiments showed the lowest frequency torsional mode's damping ratio to be small but non-zero, meaning a small amount of energy can be dissipated from the blade [12]. This small damping ratio also justifies the need for added blade damping.

Although not shown here, the same analysis was performed on the tests involving the Mylar membrane blade. Its FFT showed a strong peak at 0.535 Hz and SOCIT reported a mode at 0.534 Hz with 0.005% damping ratio. These results match the flap and twist mode of the finite element prediction for the blade membrane at 0.53 Hz.

As shown in Table 2.1, the linearized damping constant, d, used in the simulations is 2e-6 Nm^2s/rad. This value for d was chosen based on the experimental results and is far less than the previous value used in Guerrant's model. By choosing a lower damping constant, the controller design will have an added factor of safety in case the damping ratio keeps decreasing with pressure.

Overall, the modal parameter characterization experiments drove the selection for the damping constant used in the simulations for the control design. The experimental testing procedure

Table 2.4: SOCIT results for rope ladder blade

Frequency (Hz)	**Damping (%)**
0.582	0.004
1.743	0.012

was refined by determining the best input signal to use with the hardware and software available. A user defined sine impulse yielded clean free decay data over long, continuous durations of time. However, changes in the data acquisition hardware and software could be made to allow for a decaying exponential envelope to determine the damping constant instead of relying on SOCIT. In addition, more time could be devoted to the actuator design to produce separate flap and twist motion. In the future, two independent (not attached) piezoelectrics could be located at each corner of the blade, where their in-phase vibrations could produce flap motion and their out-of-phase vibrations could produce twist motion. Ultimately, the modal parameters for a combined flap and twist mode were determined for both blade types but these changes in the experimental process could yield more confident results.

Chapter 3

Proximal Blade Twist Feedback Control Design

As discussed earlier, the control systems proposed by MacNeal, Guerrant and Blomquist do not account for the friction in their systems. Since the blade only needs small control torques, on the order of 2 μNm, the friction torque dominates, causing no root motion and therefore, no blade twist. The following diagrams, Figures 3.1 - 3.3, show the mechanical configurations of each idea (without the control laws) and highlight the friction in each system. In theory, the systems will

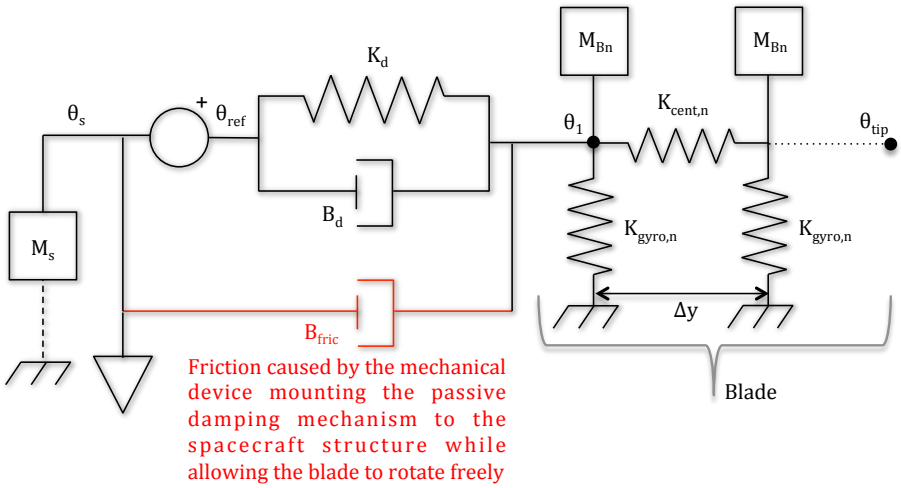

Figure 3.1: Lumped parameter model of MacNeal's passive controller with friction

add damping to the blade if friction is ignored but in practice, these systems will not be able to overcome friction.

MacNeal's passive controller, in Figure 3.1, consists of a mechanical damping device comprised of a spring and damper in parallel, K_d and B_d, respectively. Following the diagram from left to right,

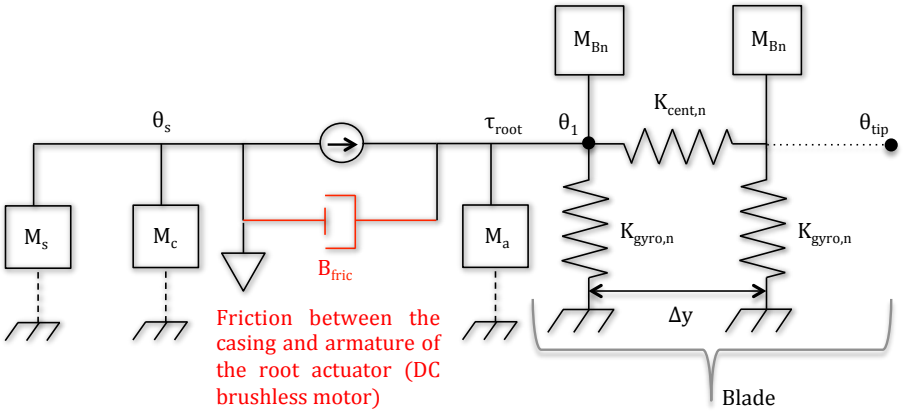

Figure 3.2: Lumped parameter model of Guerrant's active controller with friction

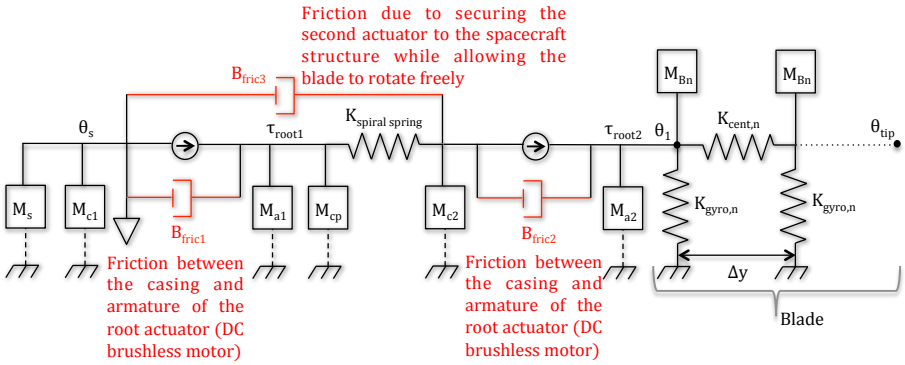

Figure 3.3: Lumped parameter model of Blomquist's active dual actuator controller with friction

the spacecraft's mass is denoted by M_s and twist by θ_s. A position source generates the reference twist input, θ_{ref}, which is grounded to the spacecraft structure along with the the damping device. The friction in the system acts across the damping device, labeled B_{fric}. There must be something limiting its degrees of freedom since it only needs to damp the unwanted twist motions in the blade. Therefore, any mechanical device used to mount the passive damping mechanism to the spacecraft structure, while allowing the blade to rotate freely, will add friction to the system. θ_1 is the root blade twist and the blade is represented by lumped mass and spring parameters for each element, M_{Bn}, $K_{cent,n}$ and $K_{gryo,n}$. More specifically, the centrifugal tension between elements is represented by $K_{cent,n}$ and the gyroscopic stiffness that causes the blade to be flat in the rotation plane is $K_{gyro,n}$. The spanwise distance between each element is given by Δy.

In place of the position source and passive damping device, Guerrant uses a root actuator or motor, shown in Figure 3.2. The actuator is a torque source that generates the root input torque to the blade, τ_{root}. In a traditional DC brushless motor, which would be used for space applications, there are permanent magnets located in the motor. The mass of the motor casing is given by M_c and is grounded to the spacecraft structure. Inside the casing, there is a spinning electromagnetic armature that torques the output shaft, which is connected to the blade. The mass associated with the armature is M_a. The friction at the root actuator is due to the bearing system that allows the armature to spin and magnetic hysteresis between the casing and armature.

Figure 3.3 shows Blomquist's dual actuator control system. The main and secondary actuators are modeled the same way as Guerrant's root actuator. However, the first is connected to the second with a coupler, M_{cp}, and a spiral spring, $K_{spiralspring}$. Friction is present in both the actuators, labeled B_{fric1} and B_{fric2}. There is a third friction term, similar to the one in MacNeal's model, that is due to the restriction of motion of the spiral spring and secondary actuator, depending on if these would be connected to the primary actuator and spacecraft structure.

As mentioned earlier, damping control does not have to be implemented at the root, as shown by Guerrant's research into RCD tip actuators. However, with the long span and the thin and flexible properties of the sail material, it would be difficult to integrate any actuator or damping

mechanism on the blade itself. For this reason, the proposed control design uses a root actuator for active feedback control. Mechanically, it is the same as Guerrant's root actuator control system shown in Figure 3.2 but instead of only feeding back a signal of blade root twist, θ_1, the differential twist at a proximal point on the blade, $\theta_6 - \theta_1$, is also sampled and fed back to the controller. Figure 3.4 shows a simplified block diagram of the proximal blade twist feedback control design. The inner

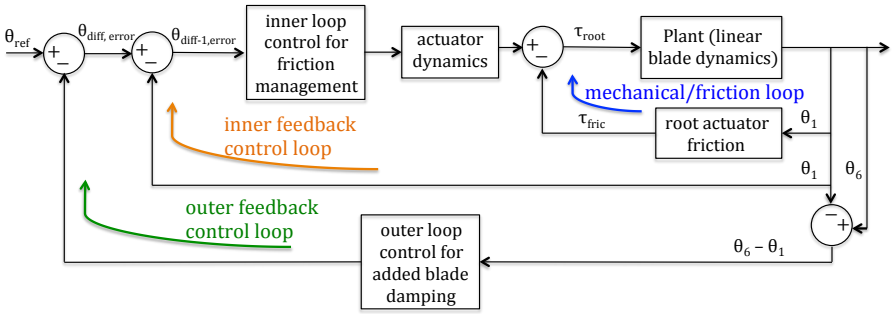

Figure 3.4: Simplified block diagram of the proximal blade twist feedback control design

control loop, that feeds back θ_1, uses a high gain controller to dominate the large friction torque, τ_{fric}, and provide good root tracking, meaning θ_1 follows the reference input θ_{ref} with minimal error. The outer feedback control loop adds blade damping by "softening" the root impedance. The following section will discuss how the large friction torques are handled as well as how the friction model was implemented in the simulations.

3.1 Friction Model

To reiterate, the active control approach still suffers from sensitivity to friction at the root mechanism. This can be addressed in three ways. First, the friction can be eliminated with magnetic (non-contact) bearings, depicted in Figure 3.5 but adds complexity to the integration of the root actuator to the blade. Second, a friction model can be used to estimate and "cancel" friction torques, shown in Figure 3.6. This method works well for linear viscous friction but could cause huge destabilizing gains if used with other kinds of friction. In addition, modeling errors could cause instabilities. Thirdly, Figure 3.7 uses high gain feedback control to "swamp out" friction

torques with feedback torque corrections. The third method is the approach taken in the control

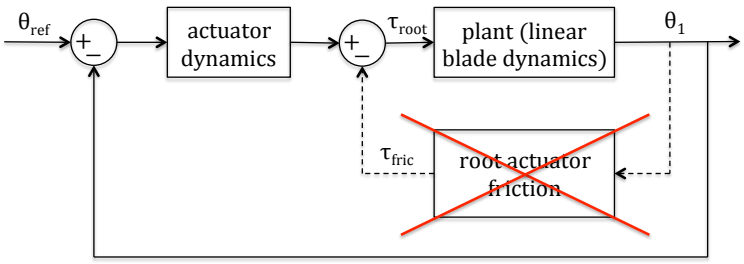

Figure 3.5: Eliminating friction with magnetic bearings

system. The inner feedback control loop uses a high gain, k, that enlarges the root input torque, τ_{root}. By using a feedback signal, τ_{root} keeps growing in magnitude until it dominates the friction torque, τ_{fric}, and is able to move the root. However, this approach does not allow active damping to be added to the blade, which is the responsibility of the outer control loop and will be discussed later in the chapter.

Nonlinear friction consists of static, kinetic and viscous friction, all shown as a function of velocity in Figure 3.8. Static friction, or stiction, is the friction between two solid objects that prevents them from moving relative to one another until some threshold of force parallel to the objects is overcome. As shown by the figure, the velocity remains zero until the force is large enough, allowing the object to move. Once the object begins sliding along the surface, kinetic, or sliding, friction ensues. The magnitude of kinetic friction remains constant as velocity increases. When kinetic friction is present, energy dissipation occurs in the form of Coulomb damping. The linear viscous friction force can act between two lubricated solids, a solid and a liquid, or two liquids. Its magnitude is linearly proportional to the relative velocity between two substances [14].

This friction model is not compatible with the numerical integration techniques used by Simulink to generate the time simulations. Therefore, a simplified model was developed using the specifications for the root actuator used at NASA Langley for blade characterization tests, which is similar to the root actuator used in the HELIOS (High-Performance, Enabling, Low-cost, Innovative, Operational Solar Sail) design. HELIOS is a collaborative small scale heliogyro demonstrator

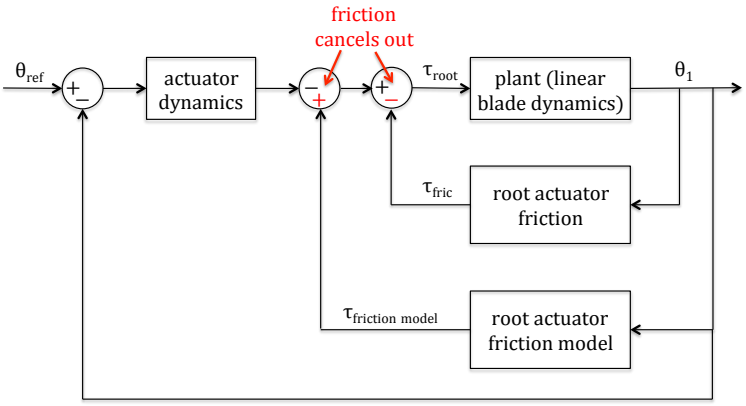

Figure 3.6: Canceling friction with friction model

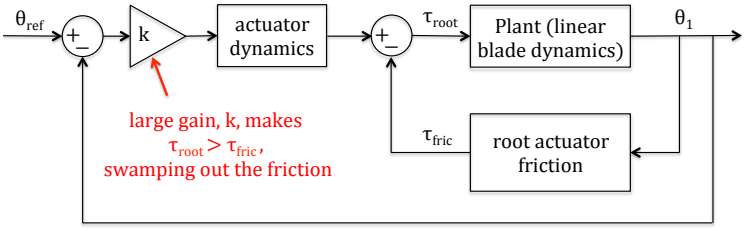

Figure 3.7: Swamping out friction with high gains

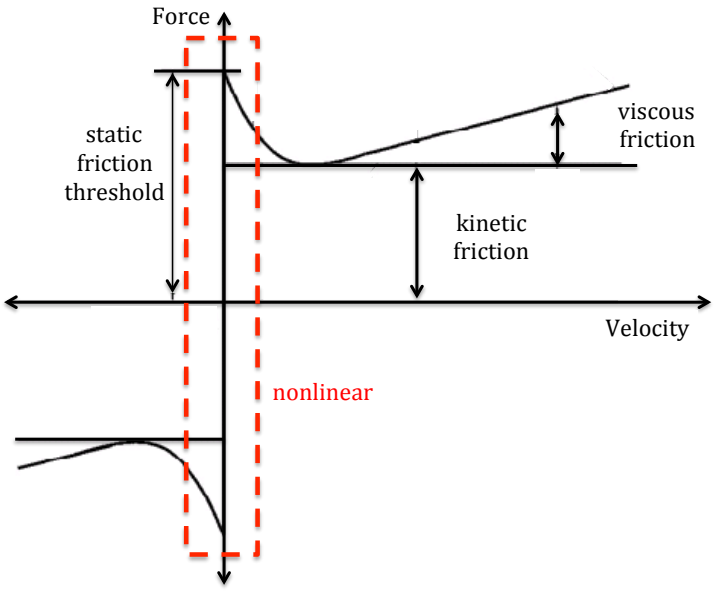

Figure 3.8: Nonlinear friction [13]

between NASA Langley, JPL and the University of Colorado at Boulder. The MAXON EC32 brushless motor specifications are shown in Table 3.1.

Table 3.1: Root actuator (MAXON EC32 brushless motor) parameters [15]

Terminal resistance (R_m)	13.7 Ω
Torque constant (k_τ)	26 Nm/A
Gear head ratio (N)	531:1
No load current (I_0)	36.9 mA
Rotor (armature) inertia (J_a)	0.16 kgcm^2
Mechanical time constant (τ_m)	20 ms
Viscous Friction Coefficient (B_m)	7.85 Nms/rad

It is important to note that the motor has a 531:1 gear ratio. The motor shaft, located before the gear, will have less torque and be spinning faster. After the gear, the torque will be 531 times greater and the shaft will be spinning 531 times slower.

Figure 3.9 shows the simplified friction model used in the simulations. To avoid the nonlinearity in Figure 3.8, the linear viscous damping from the motor is assumed to be present for small angular velocities. Since the model of the friction torque at the blade root, τ_{fR}, is desired, and not the motor friction torque, τ_{fM}, the viscous friction coefficient, B_m, must be multiplied by the gear ratio squared, N^2, to generate the slope for the friction torque at the root. Once the blade starts moving with larger angular velocities, the limits for the kinetic friction at the root are given by the motor friction torque multiplied by the gear ratio. The motor friction torque is calculated with the equation $\tau_{fM} = k_\tau I_0$ and the parameters listed in in Table 3.1. Although the simplified friction model ignores the affect of stiction, it still incorporates realistic magnitudes of friction into the simulation for the root actuator. The simplified model can now be used to design and implement the proximal blade twist feedback control design to show the concept has merit before proceeding with a more complex friction model. The next section describes the inner feedback control loop design and illustrates how the friction model and motor dynamics are incorporated into the full system block diagram.

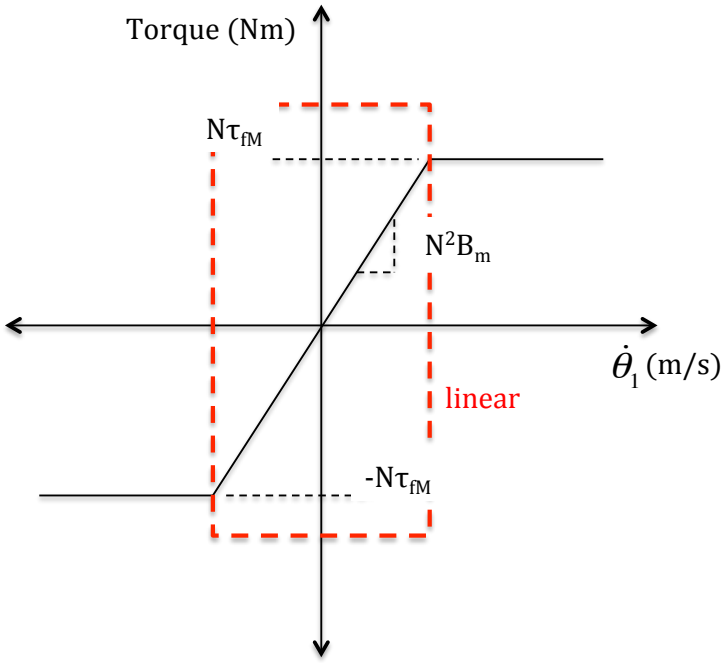

Figure 3.9: Simplified friction model

3.2 Inner Control Loop Design

The design of the control system began with the inner feedback control loop, designed to overcome the friction in the root actuator and to provide good root tracking. Previously shown in Figure 3.4, the inner control loop consists of the blade dynamics plant, the actuator or motor dynamics and the high gain controller. The blade dynamics, as discussed in section 2.1, take a root torque input and produces θ_1, θ_6, $\dot{\theta}_1$, and θ_{tip}. The motor dynamics are modeled for the direct current brushless motor, whose parameters are specified in Table 3.1. As mentioned earlier, the root actuator system is mechanically the same as Guerrant's root actuator in Figure 3.2, except for the gear head. The mechnical diagram, with some modifications, is presented again in Figure 3.10 to explain the motor dynamics model. The electromagnetic torque, τ_a, is given by the equation,

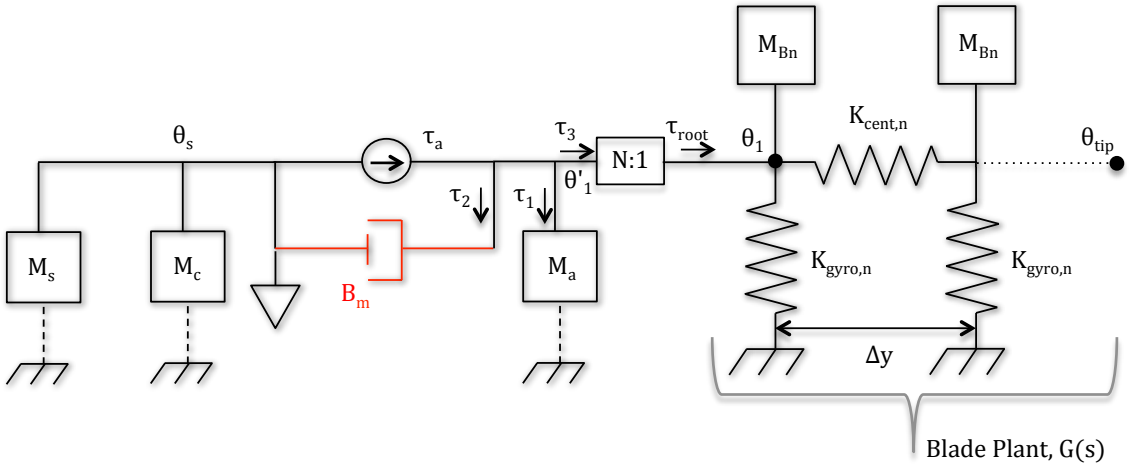

Figure 3.10: Lumped parameter model for inner control loop

$$\tau_a = k_\tau I_m, \tag{3.1}$$

where I_m is the motor current. τ_1 is the torque due to the rotational acceleration of the rotor armature inertia and is shown in Equation 3.2.

$$\tau_1 = J_a \ddot{\theta}_1 \tag{3.2}$$

The torque, τ_2, and the torque of the mechanical load, τ_3, are given in the following equations,

$$\tau_2 = B_m \dot{\theta}_1 \tag{3.3}$$

$$\tau_3 = G(s)\Theta'(s). \tag{3.4}$$

$G(s)$ is the transfer function for the blade plant, without the gear, specifically $\frac{\Theta'_1(s)}{T_3(s)}$. Finally, all the torques are related through the equation,

$$\tau_a = \tau_1 + \tau_2 + \tau_3 \tag{3.5}$$

The motor driver is not shown in Figure 3.10. For the simulation, the motor is current controlled, thus producing a linear effect on the motor torque[14]. By taking the Laplace transforms of Equations 3.1-3.5, transfer functions of the motor dynamics can be used in the Simulink model.

Figure 3.11 shows the Simulink model for the inner control loop, which is a more detailed version of the block diagram shown in Figure 3.4. The actuator friction and dynamics blocks include

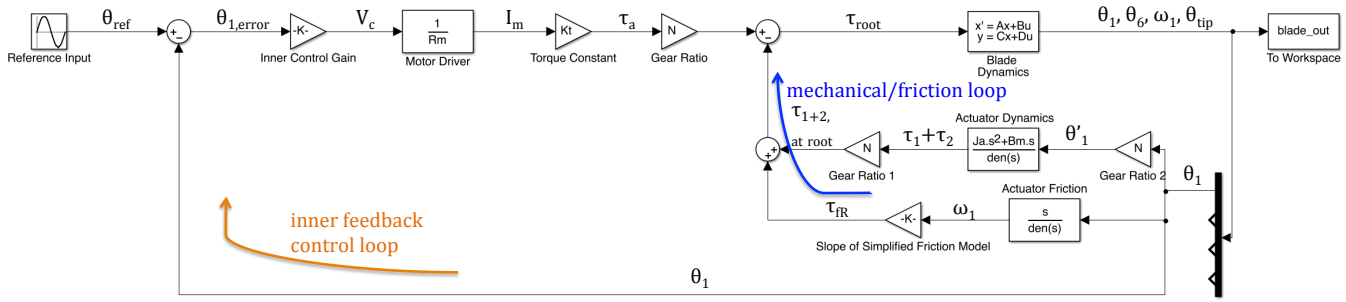

Figure 3.11: Simulink model of inner control loop

the term den(s), which is a fictitious low pass filter used to make the transfer functions proper. It is fictitious in the sense that it is not physically in the system but is a product of the simulation. The denominator has the form $\frac{1}{\omega_n^2}s^2 + \frac{1}{\omega_n}s + 1$ and the cutoff frequency for the low pass filter, ω_n, is set well above any natural modes in the system, at 100 rad/s. The actuator friction block takes the derivative of θ_1 to get ω_1 ($\dot{\theta}_1$) and then multiplies it by $N^2 B_m$ to get the linear approximation of friction in the root actuator. The kinetic friction torque limits, given by τ_{fR}, were not implemented

in the simulation because they are unnecessary. The root friction torque remains between ±0.04 Nm while the limits in the friction model are set to ±0.9 Nm.

The reference input used for the simulations is a half-p sine wave with an amplitude of 15 degrees (0.26 rad) and a frequency of $\Omega/2$ (0.0175 rad/s). Since a cyclic maneuver has the property that the entire blade pitches uniformly, the half-p was used instead so the blade's behavior was less uniform due to the difference in gyroscopic stiffness and inertia torques [3]. This research did not focus on tailoring the reference input to obtain a better pitch response from the blade.

The frequency response of the blade dynamics, the transfer function $\Theta_1(s)/T_{root}(s)$, is shown in Figure 3.12, along with the pole-zero map of this blade dynamics plant. One interesting charac-

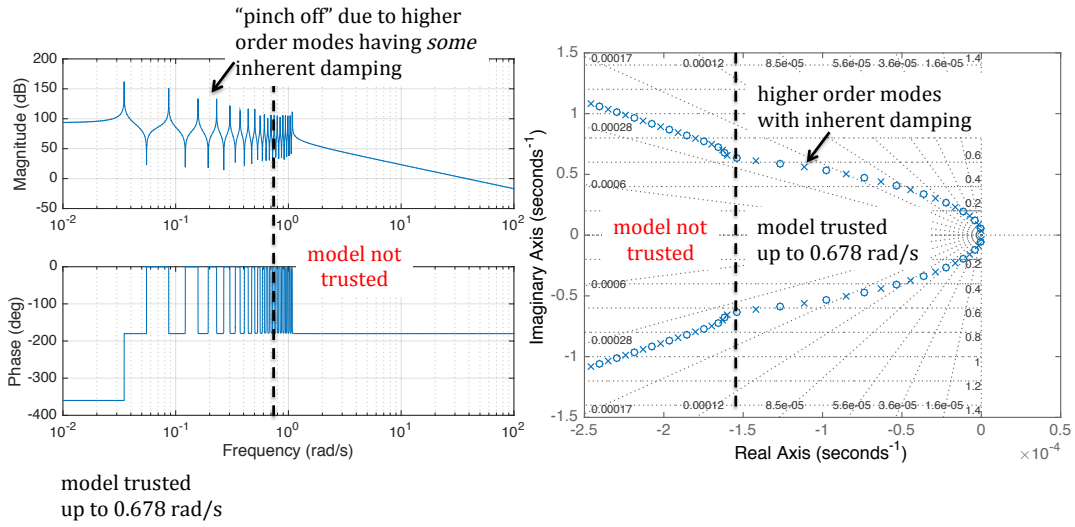

Figure 3.12: Blade dynamics frequency response and pole-zero map

teristic of the blade dynamics is that there is a visible "kink" in the trajectory of the poles and zeros of the system at 0.678 rad/s. This "kink" was discovered to be an artifact of the model because it increases in frequency as the number of elements in the model are increased. Therefore, it was assumed that the model could be trusted up to 0.678 rad/s (well above the frequency of the lower frequency blade modes) but not past it.

The blade dynamics model, uses 19 elements (20 nodes) meaning there are $N+1$ modes in the system, shown in bode plot. The magnitude of the modes reduces as the frequency increases,

which is a product of some inherent damping in the blade. The "pinch off" of these higher frequency modes will be important in the outer control loop design.

From Figure 3.11, the mechanical/friction closed loop transfer function, $\Theta_1(s)/V_c(s)$ resembles a dominant first order system, shown by the following bode plot. This closed mechan-

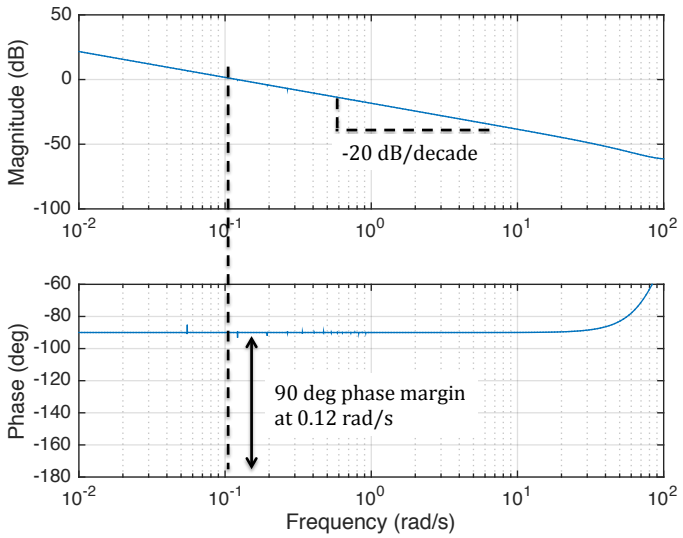

Figure 3.13: Combined blade and motor dynamics frequency response

ical/friction loop transfer function can also be referred to as the uncompensated loop gain and has infinite gain margin and a phase margin of 90 degrees at a crossover frequency of 0.12 rad/s.

When the inner feedback control loop is closed it results in the entire closed loop system, represented by the transfer function $\Theta_1(s)/\Theta_{ref}(s)$. The time simulation is implemented for 100 minutes, which is about 33 revolutions for the blade, with a gain of one for the inner control gain block. The following figure shows the $\theta_{1,error}$, or $\theta_{ref} - \theta_1$, over one-fourth the duration of simulation for easier viewing capability. The root pitch tracks the reference input fairly well but points further out on the blade, such as θ_6 and θ_{tip}, are effected by higher frequency modes and have a hard time tracking the root. The exact error at θ_1 is shown in Figure 3.15. Here, there is a steady error of 0.037 radians.

With the large gear reduction, the root actuator's torques are amplified and are able to pitch

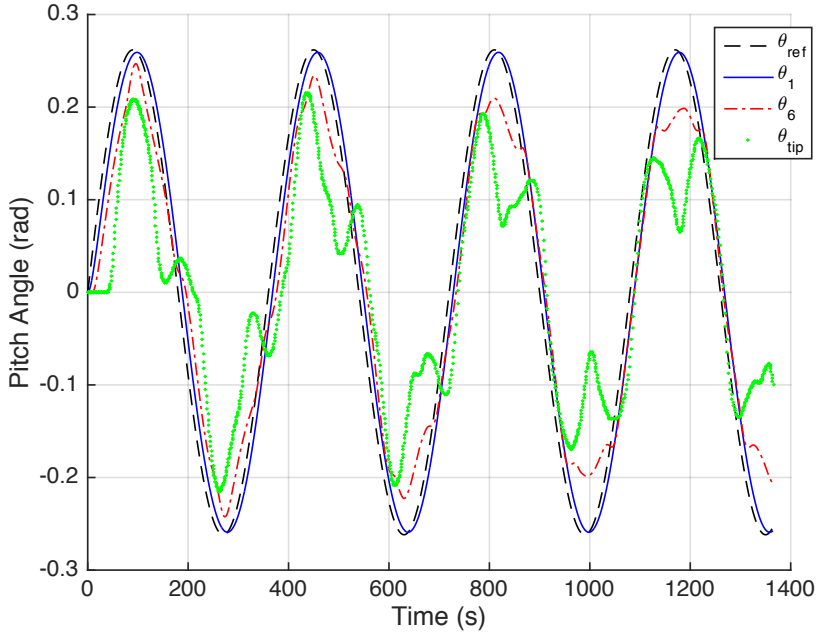

Figure 3.14: Time history for inner control loop with unity inner control gain block

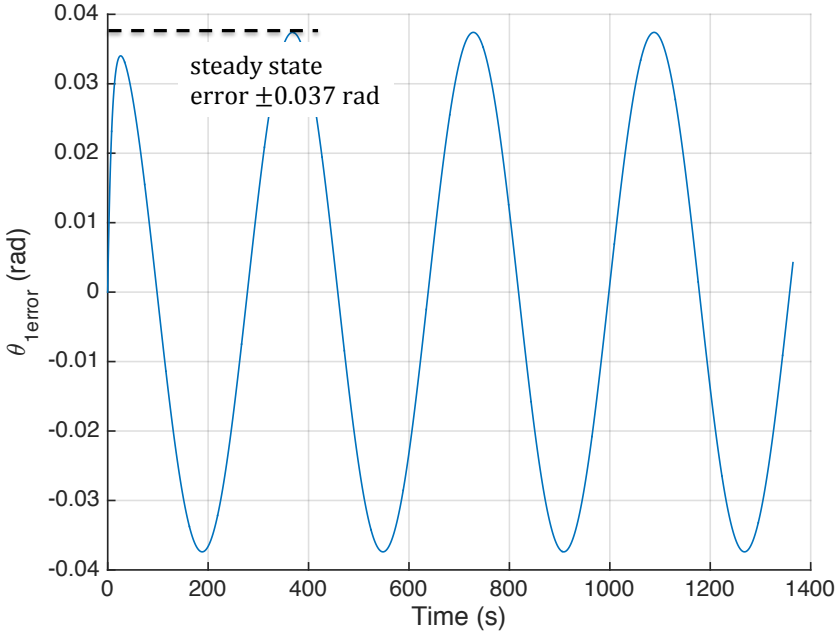

Figure 3.15: Inner control loop $\theta_{1,error}$ with unity inner control gain block

the blade, even in the presence of friction. There is no strict requirement on root tracking, although it is known that a larger inner control gain will improve root tracking. However, it will also effect the outer feedback control loop once added. For this reason the outer feedback control loop was designed in parallel with the inner control gain.

So far, the inner feedback control loop with unity gain provides good root tracking performance while managing root friction torques but it does not supply the blade with damping. The root actuator and position feedback control law essentially create a position source at the blade root. For this reason, the impedance is very high from the blade looking back at the root, meaning it takes a lot of effort, or torque, for little to no motion. High impedance makes the root actuator "stiff" meaning it cannot extract, or dissipate, any energy from the blade as excitation waves travel towards the root. Instead, those waves will bounce off the root actuator. However, by sensing and feeding back the differential twist at a proximal point on the blade, the root impedance can be reduced, allowing energy to be dissipated and thus adding damping to the blade.

3.3 Outer Control Loop Design

The purpose of the outer feedback control loop is to add damping to the blade while maintaining good root tracking. The Simulink model of the full system, with both the inner and outer feedback control loops is shown in Figure 3.16. The outer control loop feeds back the the differential twist measurement, which causes the non-collocated issue discussed in Chapter 2. The uncompensated outer loop gain, $\dot{\Theta}_6 - \dot{\Theta}_1(s)/\Theta_{diff,error}(s)$, illustrates the nature of the non-collocated problem, shown in Figure 3.17 Nyquist plot. The higher frequency circles along the positive imaginary axis are due to the non-collocated sensing and make the controller design challenging. Both the higher frequency circles and the lower frequency circles, along the negative imaginary axis, must be managed by the controller simultaneously.

The uncompensated loop gain gives insight into the behavior of the closed loop system. Without some form of compensation, the blade will become unstable. Ways to add stability include reducing the size of the circles through the proper gain or rotating the circles through some form

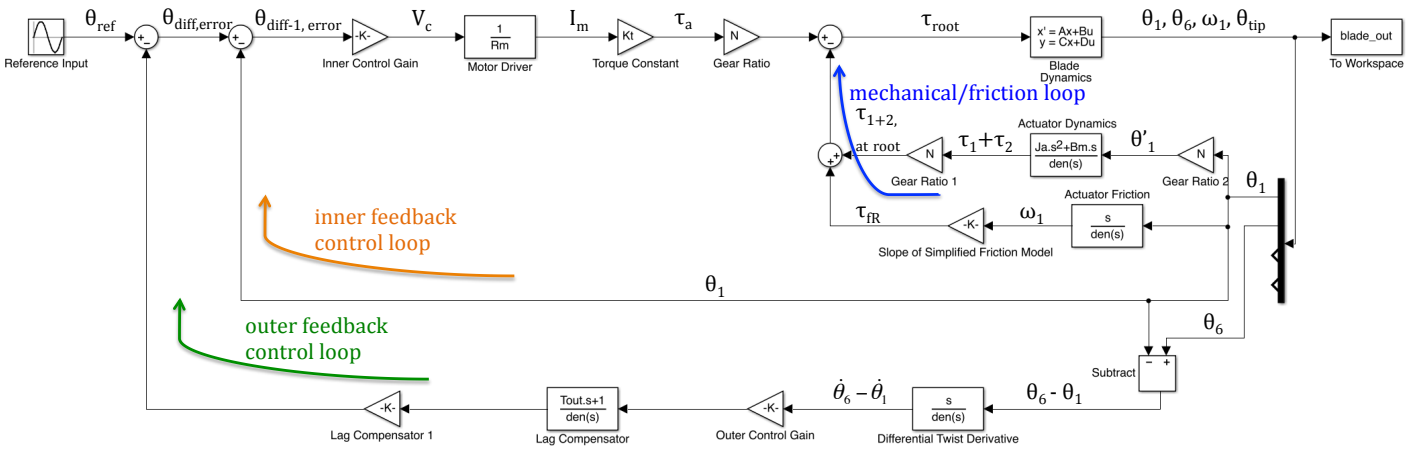

Figure 3.16: Simulink model of outer control loop

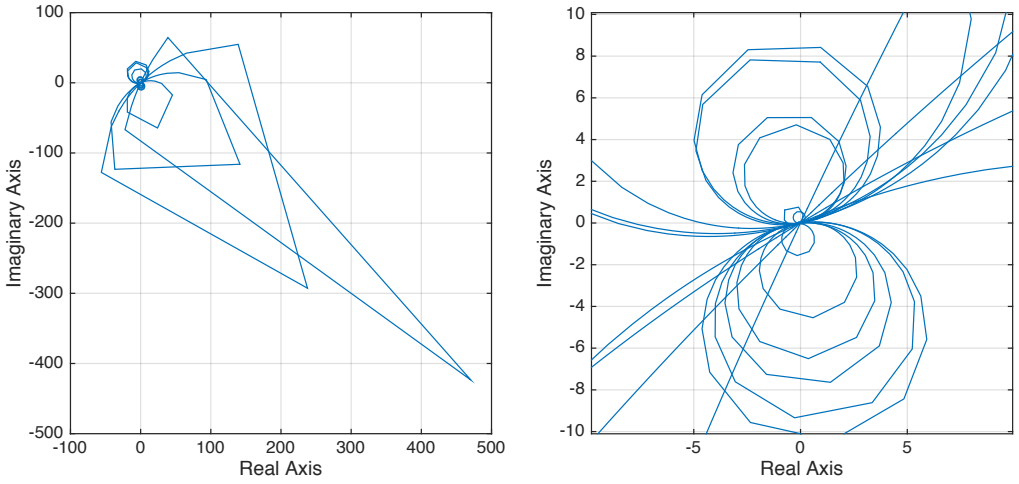

Figure 3.17: Uncompensated outer loop gain, right plot showing zoomed in view

of lead or lag compensation. In this case, both of these methods were used to yield the stable compensated outer loop gain whose Nyquist plot is shown in Figure 3.18. On the left, the full plot

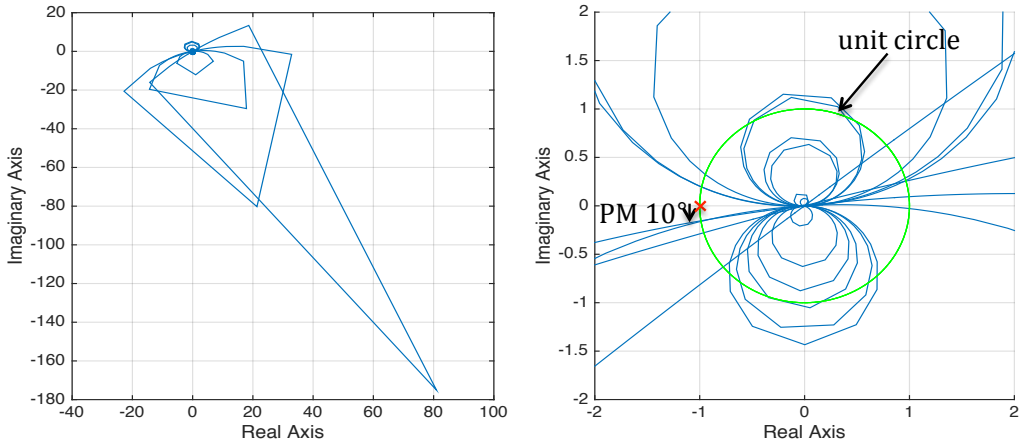

Figure 3.18: Compensated outer loop gain

is shown with all the circles. The outermost circles for the lower frequencies are only jagged due to the number of points plotted over the frequencies. The general outline is apparent but they will become more circular as the data points are increased. The right plot depicts a zoomed in view of the Nyquist plot with the unit circle drawn for reference. A gain of 0.4 was used to shrink the size of the circles and a lag compensator was used to rotate the circles clockwise. This provides infinite gain margin and a phase margin of approximately 10°.

Next, the performance of the full closed loop system is analyzed with the time histories. With the outer feedback control loop, the root tracking remains the same as the inner feedback control loop on its own. Figure 3.19 shows the same steady state root tracking error of 0.037 radians.

To illustrate the dominance of friction in the control design, Figure 3.20 compares the root friction torque, τ_{fR}, to the root torque, τ_{root}. When both are shown on the same scale it appears as though τ_{root} is zero, however Figure 3.20(b) shows the true scale of τ_{root} to be around 10 μNm. To overcome the large friction torques, the root actuator requires a certain amount of power to generate the root torques desired by the control system. The average power consumption can be

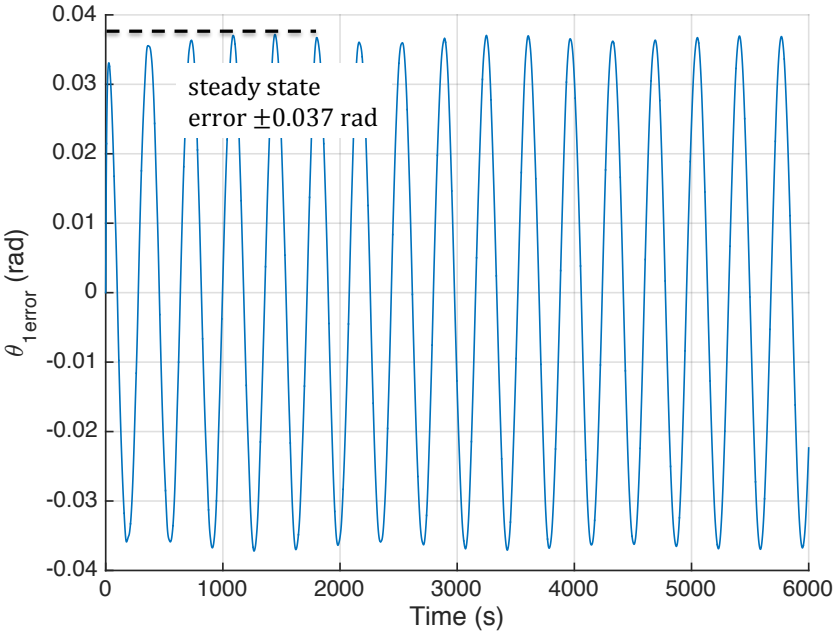

Figure 3.19: Outer control loop $\theta_{1,error}$

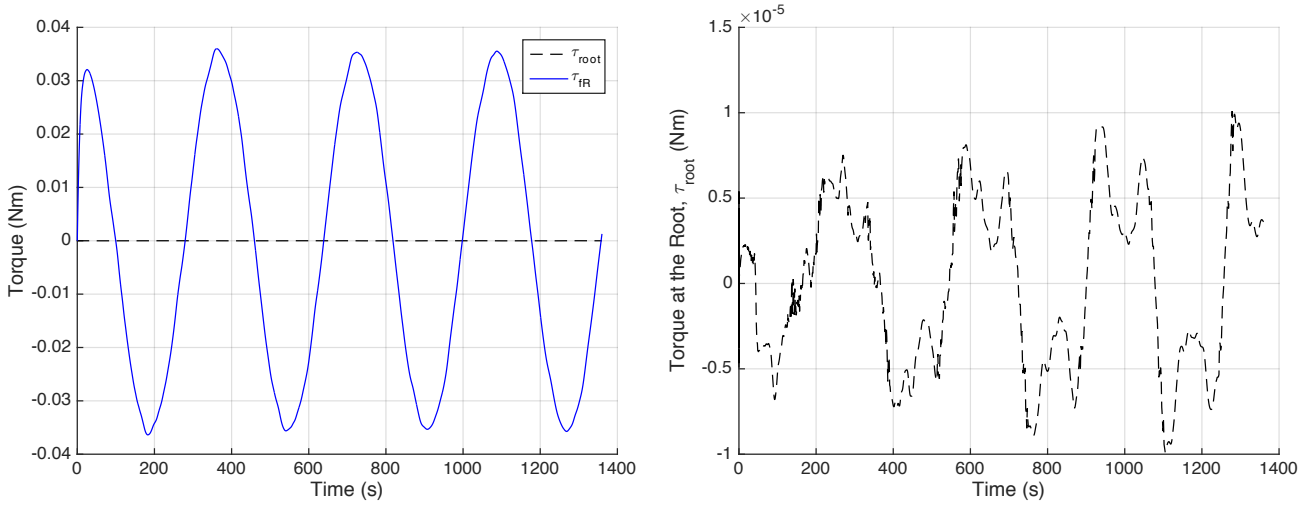

(a) (b)

Figure 3.20: (a) Comparison of friction torque at the root and root torque and (b) root torque only

calculated as,

$$P_{avg} = \int_{t_0}^{t} V I \, dt \tag{3.6}$$

With only the inner control loop implemented, the average power is 0.232 W compared to 0.237 W consumed with both the inner and outer control loops functioning. The overall power consumption of the root actuator control system will need to be considered and proven to be reasonable for a real heliogyro mission.

The most encouraging result is the time history of θ_{tip}, seen in Figure 3.21. As mentioned

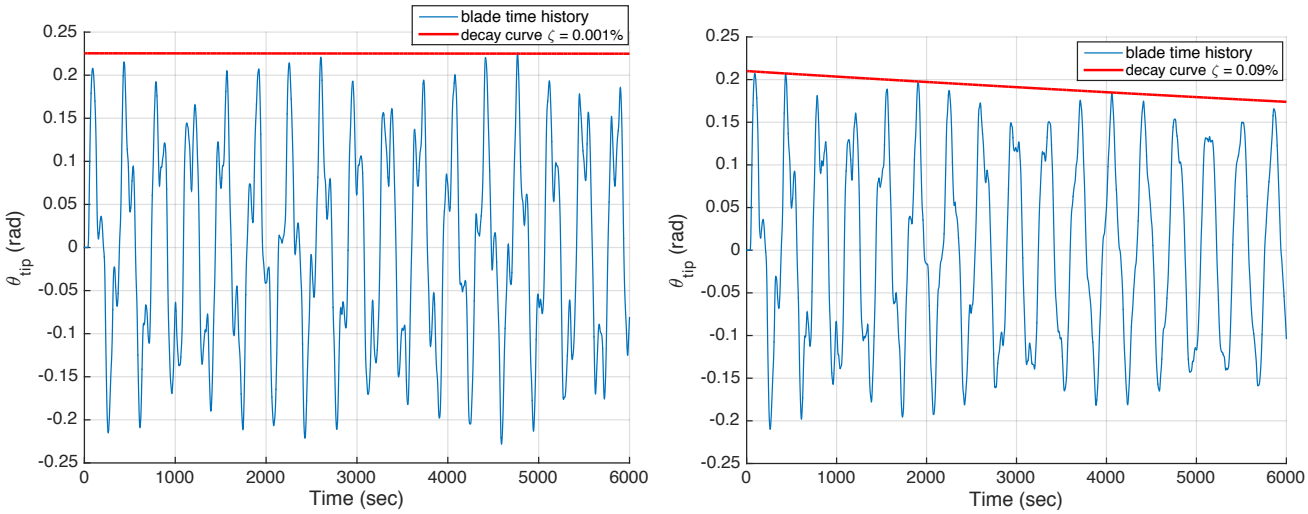

Figure 3.21: Blade tip pitch response with (a) inner feedback control loop only and (b) outer feedback control loop

earlier and depicted here, the inner feedback control loop cannot provide blade damping. However, with the proximal differential twist measurement, the damping ratio of the lowest frequency twist mode increases from 0.001% to 0.09%, which is two orders of magnitude greater. The added damping may still seem minor but when compared to a realistic heliogyro mission, the added damping is greatly beneficial. If a simple sun synchronous orbit at an altitude of 1100 km is considered for a heliogyro mission, then the orbital period is approximately 6427 seconds. The time constant associated with the lowest frequency twist mode is 318 seconds. Therefore, the rate of decay for that mode is only about 5% of the total orbital period, proving that for the long

duration missions of the heliogyro, this is a substantial amount of damping. In addition, it is also the first sign that friction in the root actuator can be addressed in a successful way. With more time to spend optimizing the controller design and the proximal sensing position along the blade, the added damping could be increased further.

It has been shown that it is possible to use a position-source root pitch controller to "swamp out" the friction in the root actuator and then wrap an outer loop to add damping to the blade by sensing differential twist outboard of the blade root. In order to instill confidence that this control design is physically realizable, the idea for the proximal differential twist sensor must be feasible. The feasibility of this sensor and measurement will be addressed in the following chapter.

Chapter 4

Photogrammetry Model for Proximal Differential Twist Sensor

Sensing differential twist at a proximal point on the blade allows damping to be added to the blade through feedback control of this measurement. Since the main goal for this research is to design a physically realizable control system, the sensing of this differential twist must also be physically realizable. Therefore, a photogrammetry model is developed to prove differential twist can be measured outboard of the blade root and the resolution of the differential twist measurement will not hinder the control system performance. In addition, the physical system will have a sensor to measure root pitch angle, most likely a rotary encoder located on the root actuator. Due to the prevalence of these sensors in space applications, the implementation of the root actuator pitch sensor will not be addressed in this master's thesis.

Figure 4.1 conceptualizes the layout of the camera sensor relative to the blade and defines the coordinate systems used in the model. The camera is mounted to the blade root and will pitch

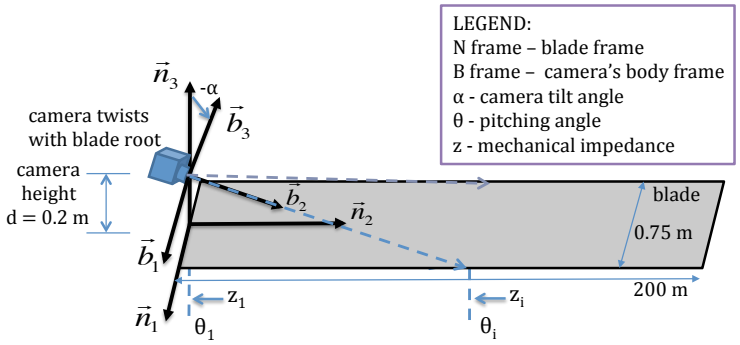

Figure 4.1: Photogrammetry model setup

as the blade pitches, thus measuring the differential twist between an outboard point and the root, $\theta_i - \theta_1$. It is located above the blade, by distance d, and angled down, with a tilt angle of $-\alpha$, so the camera's field of view encompasses the blade. The blade's frame, designated the N frame, is centered at the root, the end attached to the central hub of the spacecraft. The camera's body frame, B frame, has its origin at the lens of the camera. The desired result from feeding back the differential twist measurement is that the mechanical impedances, z_1 or z_i, are "softened" allowing energy to be extracted from the blade and thereby adding damping to the blade.

The specific camera used in the photogrammetry model is the GomSpace NanoCam C1U. This camera is used at NASA Langley for ground testing of preliminary twist controllers for a hanging blade in 1g. The camera is a modular, space-rated subsystem for nano-satellite applications, making it a realistic sensor to launch onboard a heliogyro spacecraft [16]. The specifications of the camera are listed in Table 4.1.

Table 4.1: GomSpace NanoCam C1U simulation parameters [16]

Focal length (f)	35 mm
Field of view (FOV)	9.22°
Image size	2048 × 1536 pixels
Pixel size	3.1 × 3.1 μm

First, a 200 meter three dimensional blade is defined in the N frame, shown in Figure 4.2. The blade is modeled with 51 elements, allowing the differential twist to be calculated for each element. The entire width of the flat blade is visible in the camera's large field of view from eight meters away from the root until the blade tip. For the photogrammetry model, the camera is sensing the differential twist a quarter of the way down the blade span at approximately 52 meters. The camera will have better resolution closer to the blade root but there will be less differential twist. If the measurement is taken further out, the resolution will be worse but there will be more differential twist. This proximal measurement point is chosen as a starting place and has not been optimized to enhance the blade damping but could be in the future.

The blade shape will not remain flat in the camera's field of view. The two forms of blade

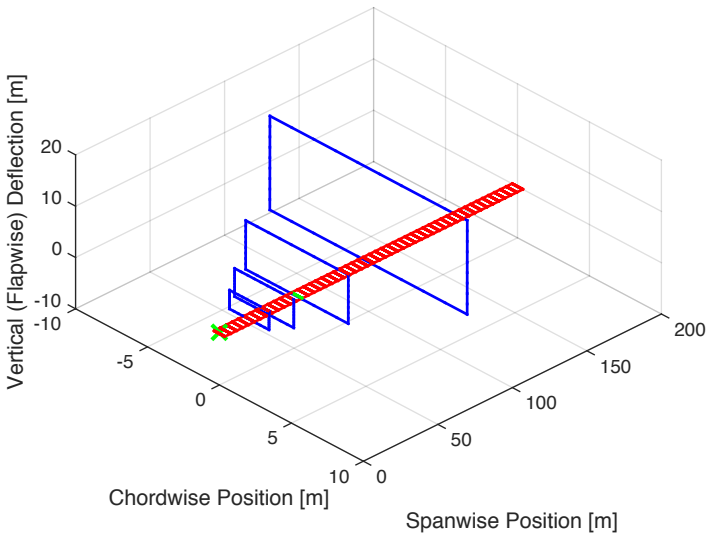

Figure 4.2: 3D blade model with camera's 2D field of view in N frame

deflection considered in the photogrammetry model are vertical deflection and blade twist. The vertical (flapwise) blade deflection, denoted as w, is caused by solar radiation pressure normal to the blade surface. It is a function of local coning angle, β, given in the following equation.

$$\beta = \frac{\partial w}{\partial r} = \frac{1}{\sigma_r} \int_r^R \frac{p_n}{t}\, dr = \frac{2p_n}{t\rho\Omega^2(R+r)} \tag{4.1}$$

The variable r (m) is the spanwise distance from the axis of rotation. σ_r (Pa) and p_n (Pa) represent the spanwise stress and normal pressure, respectively. The blade thickness and density are denoted t (m) and ρ (kg/m^3). Ω (rad/s) is the heliogyro spin rate [7]. By integrating Equation 4.1, the vertical deflection of the blade is obtained, depicted in Figure 4.3. The coning angle results in a

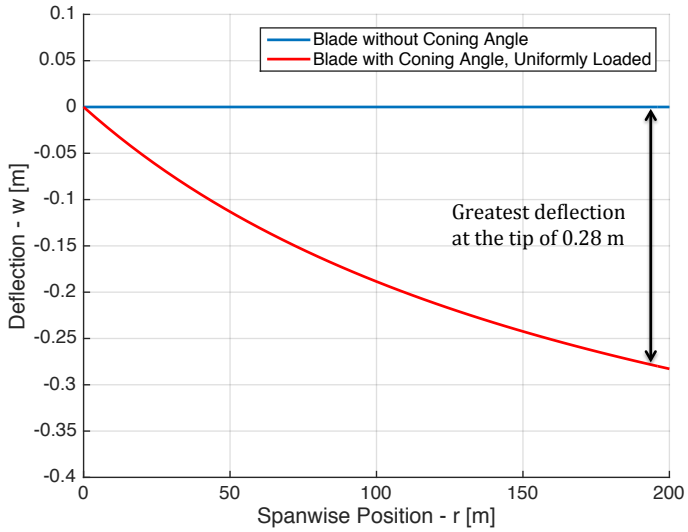

Figure 4.3: Deflection due to solar radiation pressure

tip deflection of 0.28 meters.

Next, the blade twist is considered in the photogrammetry model. Collective and cyclic maneuver twist profiles are generated for the blade. The maneuver profiles in Figure 4.4 show the worst case nonlinear blade twist without added tip mass or edge reinforcement, which is why the cyclic profiles do not follow the same trend for all amplitudes. The twist profiles are implemented in the photogrammetry model with a rotation matrix. In Figure 4.5, $\vec{r}$ is the position vector in the N frame from the origin to any point on the edge of the blade. The differential twist, defined

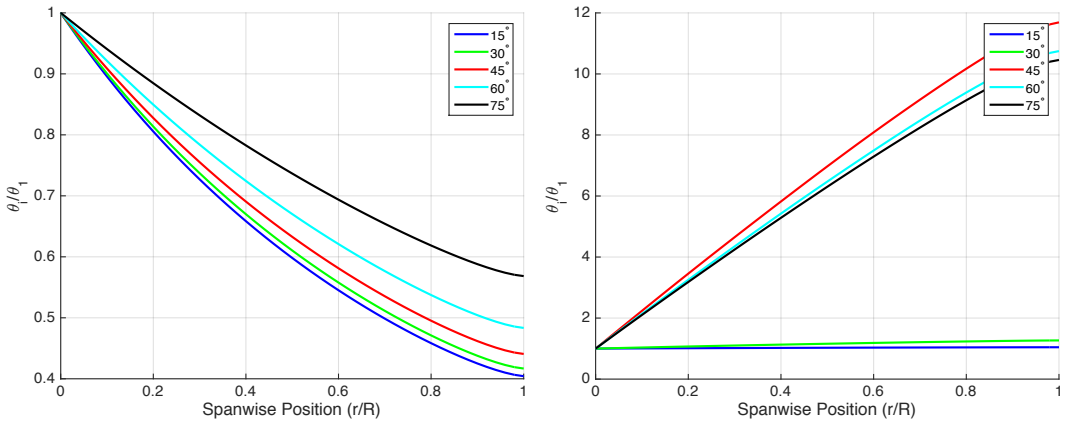

Figure 4.4: Collective (a) and cyclic (b) maneuver twist profiles [17]

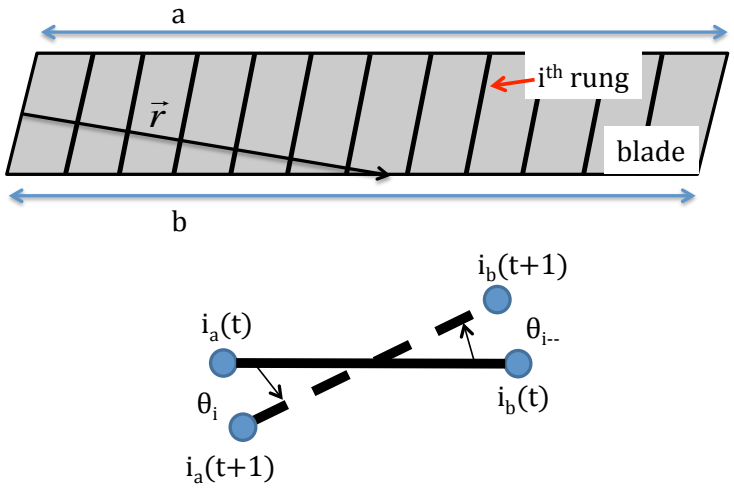

Figure 4.5: Differential twist

as $\theta = \theta_i - \theta_1$, is also depicted for each rung of the blade. The differential twist is applied to the position vector through the following transformation.

$$\vec{r}_{twist} = \begin{bmatrix} \cos\theta & 0 & \sin\theta \\ 0 & 1 & 0 \\ -\sin\theta & 0 & \cos\theta \end{bmatrix} \vec{r} \tag{4.2}$$

Figure 4.6 shows a blade experiencing both differential twist and coning angle. These blade deflec-

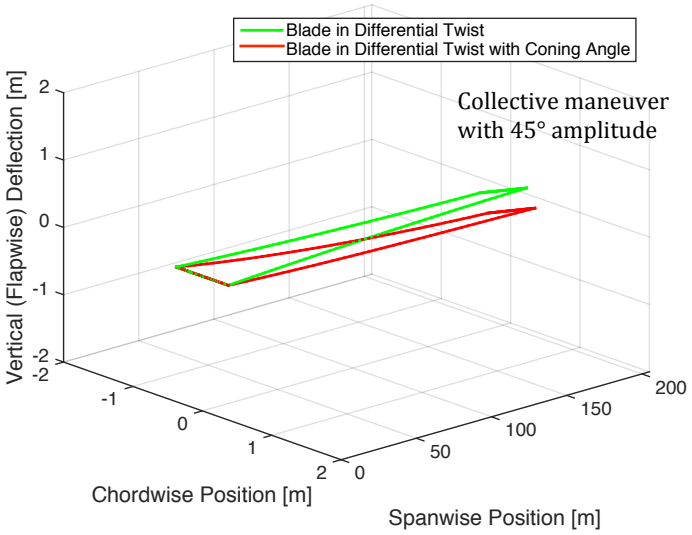

Figure 4.6: 3D blade in differential twist with coning angle

tions drastically change the camera's 2D image, making them critical for model accuracy.

A flowchart of the photogrammetry model is shown in Figure 4.7. First, the coning angle is applied to the blade in the N frame followed by the differential twist using Equation 4.2. Once these blade deflections are present in the N frame, the transformation from the 3D blade image to the 2D sensor image takes place in the function BNtrans.m.

The transformation from the N frame to the B frame begins with the offset between their origins, defined as,

$$\vec{D}_N = \begin{bmatrix} 0 \\ 0 \\ 200 \end{bmatrix} \tag{4.3}$$

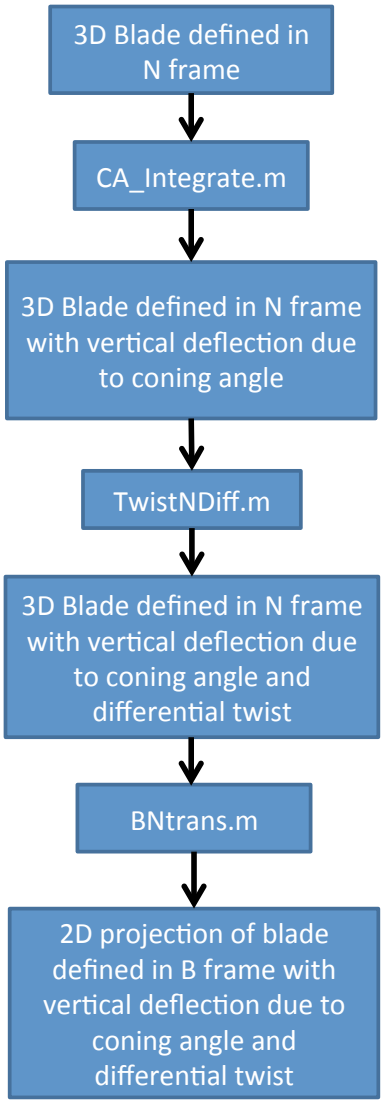

Figure 4.7: Code implementation flowchart

in millimeters. If starting with a vector in the N frame, ${}^{N}\vec{r}$, the offset is subtracted before applying the rotation matrix to yield the vector in the B frame, seen in Equation 4.4.

$$ {}^{B}\vec{r} = \begin{bmatrix} 1 & 0 & 0 \\ 0 & \cos\alpha & -\sin\alpha \\ 0 & \sin\alpha & \cos\alpha \end{bmatrix} ({}^{N}\vec{r} - \vec{D}_N) \tag{4.4} $$

Finally, the thin lens approximation is used to project the 3D image onto the 2D sensor plane, described in Figures 4.8 and 4.9. The boxed equations are used in the function BNtrans.m. The

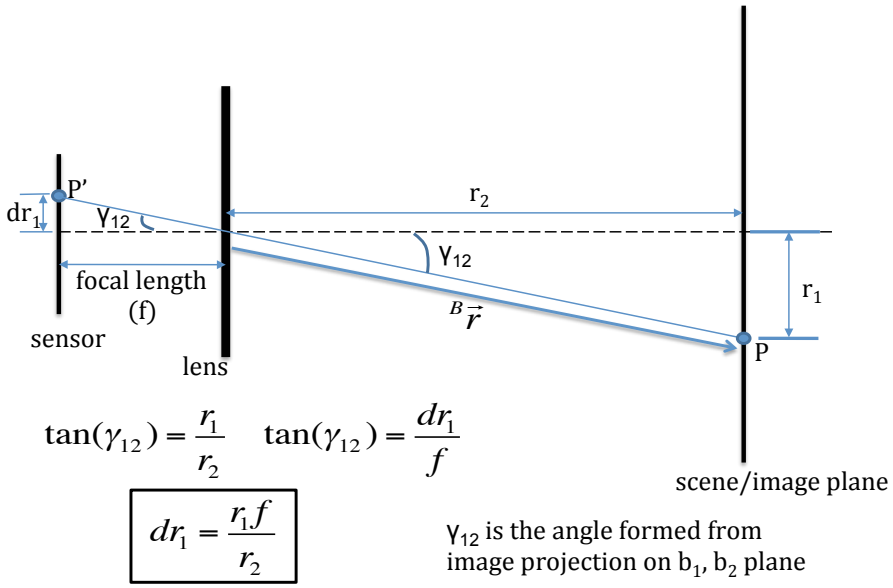

Figure 4.8: Top down view in B frame of 3D to 2D projection

equation $\tan(\gamma_{12}) = \frac{dr_1}{f}$ (or the equation for $\tan(\gamma_{23})$) can be used to calculate the resolution of the camera. From Table 4.1, a pixel is 3.1 $\times$ 3.1 μm (0.0031 $\times$ 0.0031 mm) and the focal length, f, is 35 mm. To find how many degrees a single pixel can resolve, γ_{12} is solved for, given that dr_1 is the width of a pixel. The calculation shows the camera can resolve down to 0.0051°. This resolution can be used to find the differential twist resolution at the proximal point on the blade. At the 52 meter spanwise measurement point on the blade, 0.0051° of resolution corresponds to a vertical blade displacement, r_{52}, of 4.6 mm. Therefore, the differential twist is calculated as $\theta_{diff} = \arctan\frac{r_{52}}{c/2}$. The differential twist resolution is 0.71° at the proximal measurement point 52

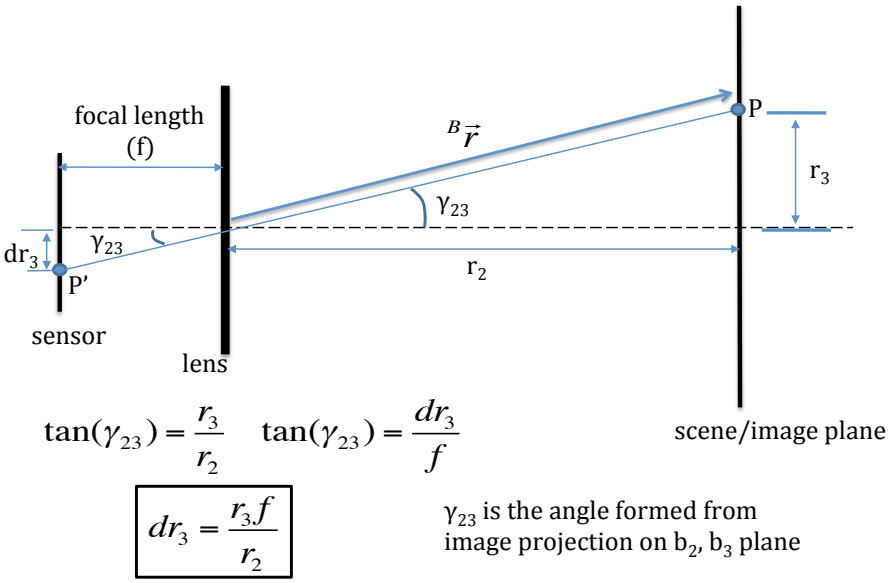

Figure 4.9: Side view in B frame of 3D to 2D projection

meters away from the blade root.

Figure 4.10 shows the sensor image for a collective maneuver at a 45° amplitude. The

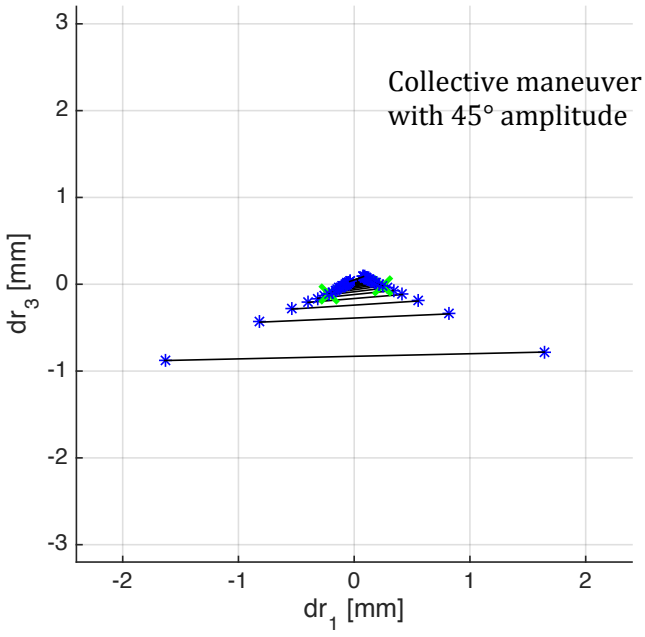

Figure 4.10: Camera's 2D view of 45° collective maneuver

measurement point at 52 meters is marked by the larger "X" markers. This 2D image shows that a camera sensor at the root can view differential twist at a proximal point on the blade. More specifically, it can resolve that differential twist measurement to 0.71°.

The affect of this sensor measurement on the control system can be analyzed by adding a quantizer block to the simulation, set to the 0.71° (0.0124 rad) resolution. Upon doing so, the controller performed well with only a slight decrease in blade damping due to the quantization. Figure 4.11 shows the decay curve, with 0.075% damping ratio, fitted to the blade tip pitch profile. The decay curve fit with no quantization present was shown in Figure 3.21. There, a damping ratio of 0.09% was used, meaning there is a 0.015% decrease in percent damping with quantization. However, even with this slight decrease, damping is still added to the blade, proving the proximal differential twist sensor in the outer feedback control loop is feasible. Again, the location of the differential twist measurement has not yet been optimized.

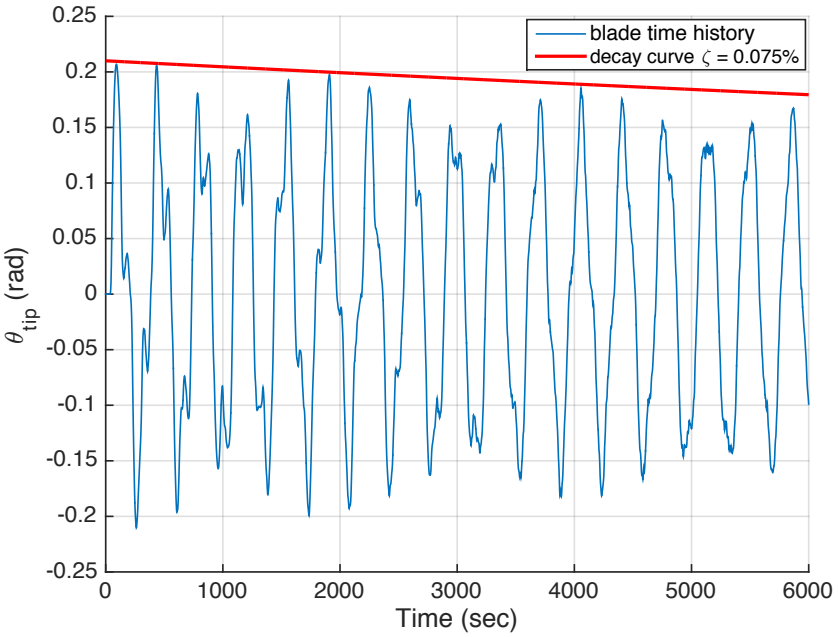

Figure 4.11: Blade tip pitch damping with quantization in outer control loop

Chapter 5

Conclusions

5.1 Impact and Significance

With very little inherent damping present in the blade, an active controller is used to damp the torsional structural modes of a single heliogyro blade. The inner feedback control loop showed it works well in the presence of friction but cannot provide any blade damping. The outer feedback control loop was able to add damping, specifically it increased the damping ratio of the lowest frequency torsional mode from 0.001% to 0.09%, two orders of magnitude greater. The photogrammetry model proved that proximal differential twist sensing with a camera at the root is feasible and not detrimental to the controller's performance. Again, this research is the first indication that a physically realizable blade root controller can deal with friction in an effective way, thus taking a step towards advancing the technology readiness level of the heliogyro spacecraft.

5.2 Future Work

The non-collocated dynamics are the key limitation of this control design. Again, the controller was not optimized to add maximum damping but could be with adjustments to the location of the differential twist measurement and other forms of compensation in the outer feedback control loop. In addition, a more complete friction model can be incorporated in future designs to instill more confidence in the practicality of the control design. Finally, future work could include a detailed analysis into the robustness of the control design to changes in the inherent blade damping and reference pitch profiles.

Bibliography

[1] D. Coulter, "A brief history of solar sails," AIAA Journal, vol. 14, pp. 766–773, 2011.

[2] C. R. McInnes, Solar Sailing: Technology, Dynamics and Mission Applications. Springer Science and Business Media, 2004.

[3] D. A. L. Daniel V. Guerrant and W. K. Wilkie, "Performance of a heliogyro blade twist controller with finite bandwidth," AIAA GNC/AFM/MST/ASC, 2012.

[4] D. A. L. Daniel V. Guerrant and W. K. Wilkie, "Heliogyro blade twist control via reflectivity modulation," SDM Student Papers Competition, 2012.

[5] R. Blomquist, "Richard's work site."

[6] R. H. MacNeal and J. M. Hedgepeth, "Helicopters for interplanetary space flight," American Helicopter Society, 1978.

[7] R. H. MacNeal, "The heliogyro, an interplanetary flying machine," tech. rep., NASA Contractor's Report CR-84460, June 1967.

[8] R. H. MacNeal, "Structural dynamics of the heliogyro," tech. rep., NASA Contractor's Report CR-1745, 1971.

[9] R. S. Blomquist, Heliogyro Control. PhD thesis, Carnegie Mellon University, 2009.

[10] J. Thomson, "Small scale heliogyro blade high vacuum damping experiment." PowerPoint slides, 2013.

[11] J. N. Juang and L. G. Horta, "System/observer/controller identification toolbox (socit)." Open Channel Software Foundation, Evanston, IL 60201, 1997.

[12] W. K. Wilkie, "Heliogyro solar sail research at nasa," tech. rep., NASA Langley Research Center.

[13] "Translational friction." Mathworks, 2015.

[14] K. Ogata, System Dynamics. Prentice Hall, 2003.

[15] "Ec 32 flat 32 mm, brushless, 15 watt, with hall sensors." Maxon Motor, 2015.

[16] "Datasheet for nanocam c1u." GomSpace ApS., 2011.

[17] D. V. Guerrant, "Collective and cyclic twist profiles." MATLAB figures, 2014.